**Hydrothermal Venting and Mineralization in the Crater of Kick'em Jenny Submarine Volcano, Grenada (Lesser Antilles)**

Steven Carey
*Graduate School of Oceanography, University of Rhode Island*
Rene Olsen
*Graduate School of Oceanography, University of Rhode Island*
Katherine L.C. Bell
*Ocean Exploration Trust, Mystic, CT*
Robert Ballard
*Graduate School of Oceanography, University of Rhode Island*
Frederic Dondin
*Seismic Research Centre, University of the West Indies*
Chris Roman
*Graduate School of Oceanography, University of Rhode Island*
Clara Smart
*Department of Ocean Engineering, University of Rhode Island*
Marvin Lilley
*School of Oceanography, University of Washington*
John Lupton
*Pacific Marine Environmental Laboratory, NOAA*
Brad Seibel
*Department of Biological Sciences, University of Rhode Island*
Winton Cornell
*Department of Geosciences, University of Tulsa*
Craig Moyer
*Department of Biology, Western Washington University*

Prepared for Geochemistry, Geophysics, Geosystems ($G^3$)
February, 2016

## Key Points

1. Hydrothermal system of Kick'em Jenny explored using remotely operated vehicles
2. Multiple lines of evidence for phase separation of hydrothermal fluids
3. Mineralization dominated by deposition of iron-oxyhydroxides


## Abstract

Kick'em Jenny is a frequently-erupting, shallow submarine volcano located 7.5 km off the northwest coast of Grenada in the Lesser Antilles subduction zone. Focused and diffuse hydrothermal venting is taking place mainly within a small (~70 x 110 m) depression within the 300 m diameter crater of the volcano at depths of about 265 meters. Much of the crater is blanketed with a layer of fine-grained tephra that has undergone hydrothermal alteration. Clear fluids and gas are being discharged near the center of the depression from mound-like vents at a maximum temperature of 180$^o$ C. The gas consists of 93-96% $CO_2$ with trace amounts of methane and hydrogen. Gas flux measurements of individual bubble streams range from 10 to 100 kg of $CO_2$ per day. Diffuse venting with temperatures 5 to 35$^o$ C above ambient occurs throughout the depression and over large areas of the main crater. These zones are colonized by reddish-yellow bacteria with the production of Fe-oxyhydroxides as surface coatings, fragile spires up to several meters in height, and elongated mounds up to tens of centimeters thick. A high-resolution photomosaic of the inner crater depression shows fluid flow patterns descending the sides of the depression towards the crater floor. We suggest that the negatively buoyant fluid flow is the result of phase separation of hydrothermal fluids at Kick'em Jenny generating a dense saline component that does not rise despite its elevated temperature.

## 1. Introduction

Hydrothermal venting and mineralization at submarine volcanoes in subduction zones can differ significantly from the well-studied venting associated with mid-ocean ridge spreading centers [e.g. *Von Damm, 1990; deRonde et al., 2003; Hannington et al., 2005*]. These differences reflect the greater compositional diversity and higher content of primary gases in subduction zone magmas [*deRonde et al., 2003*]. In addition, the lower pressure in shallow submarine arc environments enhances the potential for phase separation of hydrothermal fluids and limits the maximum temperature of discharging fluids on the seafloor [*Drummond and Ohmoto*, *1985*; *Bischoff & Rosenbauer*,*1987*]. Hydrothermal mineralization due to phase separation has been suggested as the primary mechanism by which significant sub-surface metal deposits form based on thermodynamic and experimental studies [*Drummond and Ohmoto, 1985*; *Bischoff & Rosenbauer*,*1987*] and the important role of bacteria in facilitating precipitation of mineral phases, especially Fe-bearing ones, is become increasingly more appreciated at submarine volcanoes [*Emerson and Moyer, 2002; 2010; Emerson et al., 2010; Edwards et al., 2005; Nakagawa et al., 2005*].

Assessing the contribution of submarine arc hydrothermal activity has important implications for global ocean chemistry and for shallow-water injection of potentially biogeochemically significant components. Recent explorations in the Mariana, Tonga-Kermadec and Japanese arcs have contributed greatly to an appreciation of the significant extent and diverse nature of hydrothermal activity taking place in the Western Pacific [*Baker et al., 2008*; *Resing et al., 2009; deRonde et al., 2007*]. Extrapolations of the venting frequency along the Marianas arc suggests that the intraoceanic arc contribution to the global hydrothermal flux is 10% of that from the mid-ocean ridge system [*Baker et al., 2008*].

Kick'em Jenny is a submarine arc volcano located just northwest of the island of Grenada in the Lesser Antilles volcanic arc and is the most active volcano in the West Indies. With a summit depth of only 180 meters, Kick'em Jenny provides an interesting natural laboratory to study the activity and evolution of a young shallow submarine arc volcano and its associated hydrothermal activity. A water column survey along the Lesser Antilles arc found that the strongest evidence of hydrothermal activity occurred on the flanks of Kick'em Jenny [*Koschinsky et al., 2007*], although this study was not able to directly access the crater area due to operational restrictions. An extensive area of hydrothermal venting with gas release was discovered in the crater area during a 2013 cruise of the *R/V Brown* [*Sigurdsson and Carey, 2003*]. More recently, the *E/V Nautilus* conducted ROV explorations, high-resolution multibeam mapping, and sampling of Kick'em Jenny's hydrothermal system during cruises NA039 in 2013 and NA054 in 2014 [*Carey et al., 2014a; Carey et al., 2015*]. In this paper we report on the results of these recent cruises that define the current aerial distribution and nature of hydrothermal venting within the crater area of Kick'em Jenny. Geochemical analyses of hydrothermal deposits and gases collected in 2003 and 2013 within the crater are presented and interpreted within the context of subsurface phase separation of hydrothermal fluids as proposed for the Kick'em Jenny hydrothermal system by *Koschinsky et al.* [*2007*].

## 2. Geologic Setting

### 2.1 Lesser Antilles arc

The Lesser Antilles volcanic arc is located on the eastern edge of the Caribbean plate between the 12$^o$ and 18$^o$ N (Figure 1). Subduction of the Atlantic seafloor is occurring east of the arc at a rate of ~2 cm/yr [*Bouysse et al.,1990*]. North of the island of Dominica the arc consists of two segments: the Limestone Caribbees to the east (pre-late Oligocene volcanic activity) and the active Volcanic Caribbees to the west (Neogene activity). To the south of Guadeloupe island there is single line of volcanic centers that have activity spanning from perhaps early Eocene to the present [*Bouysse et al.,1990*]. The most voluminous subduction-related volcanism has occurred in the central part of the arc on the islands of Guadeloupe, Dominica, Martinique and St. Lucia (Figure 1).

An extensive area of sediment accretion, mud volcanoes, and chemosynthetic cold seeps lies to the east of the Lesser Antilles and includes the uplifted island of Barbados [*Westbrook, 1982; Westbrook and Smith, 1983; Olu et al., 1997*]. Magmas produced in the arc exhibit increasing strontium and lead isotopic values from north to south indicating the important role of subducted terrigenous sediment in the magma genesis process beneath the arc [*White and Deplus, 1986*]. Volcanism in the southern part of the arc on the island of Grenada has produced compositionally diverse and generally more alkalic eruptive products by fractional crystallization of two types of primary basaltic magmas [*Devine, 1995*].

### 2.2 Kick'em Jenny: structure, eruptive activity and hydrothermal venting

Kick'em Jenny (KeJ) is located just 7.5 km north of the island of Grenada in the southern Lesser Antilles (Figure 1). The first detailed bathymetric survey of the volcano in 1972 revealed a 1300 m high conical structure, constructed on the western flank of the arc with a summit crater at 190 meters depth [*Sigurdsson and Shepherd, 1974*]. Submersible dives in 1989, a few months after the 1988 eruption, revealed that the volcanic cone consisted of both pyroclastic deposits and pillow-like lava flow units [*Devine and Sigurdsson, 1995*]. Recent SEABEAM mapping of the volcano has shown that the summit cone and crater actually lie within a much larger arcuate collapse structure that opens to the west [*Sigurdsson et al., 2006*]. A debris avalanche deposit associated with formation of the horseshoe-shape collapse structure extends 17 km downslope into the back-arc Grenada Basin [*Lindsay et al., 2005; Dondin et al., 2012*] with chemosynthetic cold seeps at the distal end [*Carey et al., 2014b*].

KeJ has erupted at least 12 times since 1939 and is the most active volcano in the West Indies [*Devas, 1974; Lindsay et al., 2005*]. The last eruption occurred in 2001 and the average repose period has been about 6 years, although during the past several decades it has erupted about once every 10 years. Some of the eruptions produce surface disturbances, subaerial plumes, and minor tsunamis, whereas others have been detected only by T-phase seismic signals [*Shepherd and Robson, 1967; Lindsay et al., 2005*].

The erupted products are predominantly basaltic in composition and unusually rich in amphibole megacrysts [*Sigurdsson and Shepherd, 1974; Devine and Sigurdsson, 1995*]. One sample has the highest U-excess ($^{238}U/^{232}Th$) of any arc rock in the world, possibly due to the addition of U to the magma source by subduction-derived fluids [*Gill and Williams, 1990*]. KeJ basalts also have relatively high $^{87}Sr/^{86}Sr$ (0.70573) and high $^{206}Pb/^{204}Pb$ (19.642), as is typical for the volcanic products of the nearby Grenadines and Grenada [*Turner et al. 1996*].

Evidence of hydrothermal activity at KeJ was first recognized by recovery of a red-orange mud with high ferric oxide content [*Sigurdsson and Shepherd, 1974*] and reddish- to orange-colored bacterial mats were observed growing within the crater on volcaniclastic sediment in 1989 [*Devine and Sigurdsson, 1995*]. A water column survey cruise along the length of the Lesser Antilles discovered evidence for hydrothermal venting offshore of Montserrat, Dominica, and St. Lucia, but the strongest signal came from KeJ [*Koschinsky et al., 2007*]. Water samples from the western flank of KeJ included a hydrothermal component characteristic of the vapor phase of a phase- separated fluid with contributions from a magmatic source [*Koschinsky et al., 2007*]. In 2003, cruise RB-030-03 of the *R/V Brown* identified clear fluid venting with inferred temperatures greater than 270$^{o}$ C and vigorous discharge of gas within the inner crater of KeJ [*Sigurdsson and Carey*, *2003*], but no samples of the fluids or gases were collected at that time. Cruises NA-039 and NA-054 of the *E/V Nautilus* were designed to carry out detailed exploration and sampling of the hydrothermal system in the crater and assess the structure and morphology of the volcano in comparison to the mapping carried out in 2003.

## 3. Methods

The KeJ cone and surrounding area were mapped during cruises NA039 and NA054 with a Kongsberg EM302 multibeam echosounder system on the *E/V Nautilus*. Remotely operated vehicle (ROV) exploration of the crater and slopes areas were carried out using the 2-vehicle ROV system *Hercules* and *Argus* rated to 4000 m depth. Samples were collected by the ROV using the manipulator grab, push cores, and suction sampler (Table 1). Ultra-high resolution (cm-scale) mapping and photomosaicing of the hydrothermal vent areas were accomplished using a BlueView 1350 kHz 90-degree multibeam system, stereo cameras, and structured light laser system outfitted on the *Hercules* ROV [*Roman et al.*, *2013*]. Survey height was 2-4 meters above the bottom with 50% overlap of survey lines. Details about specific sample collection techniques and subsequent analytical methods are provided in the supplemental material (Supporting information S-1).

## 4.0 Results

### 4.1 Kick'em Jenny: structure and morphology

New multibeam mapping of KeJ in 2013 during cruise NA039 further revealed the detailed structure of the volcano's current cone (Figure 2). The 320 meter-wide crater of KeJ can be divided into three morphologically distinct regions. The first is the arcuate crater rim, which is topographically higher than the rest of the crater, and is breached in the north-northeastern sector. A minimum water depth (180 m) is found on the western side of the crater rim. The second region is a small depression located in the northwestern part of the main crater floor, referred to as the inner crater in this paper (Figure 2). This inner crater is the deepest part of the KeJ crater area with a maximum depth of approximately 265 meters. Finally, the third region is the relatively flat crater floor area south and east of the inner crater with depths of 240-245 meters.

## 4.2 Distribution and Nature of Hydrothermal Venting

### 4.2.1 Inner Crater

Hydrothermal venting at KeJ is most strongly focused within the inner crater and takes a variety of forms as shown by a high resolution photomosaic (Figures 2 and S-1). Venting consists of generally clear, shimmering fluid with or without streams of bubbles. Some of the venting occurs in isolated patches within volcaniclastic sediment or talus slopes along the inner crater margin. In other cases, fluid and gas discharges occur in hummocky areas blanketed by gray, fine-grained sediment. The strongest discharges of shimmering water and gas bubbles occur in the northwest and southwest parts of the inner crater, where venting takes place through mounds on the crater floor and along the sloping walls of the crater. At the Shrimp vent (Figure 2), named after the abundance of *Alvinocaris sp.* shrimp living within the porous sediment at the vent openings, the highest temperature recorded in clear fluids was 180$^{o}$ C. Abundant gas bubbles were also rising from multiple sites along the strongly sloping area (Figure 3a). On the crater floor the second highest temperature of 160$^{o}$ C was recorded in shimmering fluids at an oval-shaped mound with vigorous discharge of bubble streams from multiple points. The site, named Champagne vent (Figure 2), was several meters in diameter and about 50 cm in height (Figure 3b).

Lower temperature fluids (~55$^{o}$ C) are being discharged along the southeast wall of the inner crater from fragile, reddish-orange spires up to a meter or two in height (Figure 3c, movie S1). In some cases the spires are arranged in a linear fashion suggesting the control of fluid venting by faults in the inner crater wall (Figure S-1). Other areas of more diffuse flow in the inner crater can be identified by yellowish/orange bacterial mats that often have small, decimeter-scale ovoid mounds (Figure 3d).

The photomosaic of the inner crater reveals a distinctive feature of the fluid venting at KeJ (Figure 2). Downslope movement of fluid from the inner crater walls to the floor of the crater is indicated by the patterns of light-colored bacterial mats and exposure of light bluish-gray fine-grained sediment. This is best seen in the northeast corner of the inner crater where whitish bacteria have colonized an anastomosing pattern of fluid flow discharging from coarse scree at the base of the crater wall (Figure 4a, movie S2) and in the pattern of white bacterial mats occurring at the steeply sloping Shrimp vent (Figure 4b). Density measurements of vent fluid samples at different locations in the crater suggest contrasting flow behaviors are to be expected. Fluids collected on the rim of the inner crater at 222 meters depth near the reddish spires were less dense than the ambient crater water at that depth (Figure 5, Table 2), whereas fluids collected at the Champagne vent on the inner crater floor (256 meters) were denser than ambient water at that level (Figure 5).

#### 4.2.2 Outer Crater

Diffuse venting of hydrothermal fluids appears to be common in many areas of the outer crater of KeJ as evidenced by the occurrence of yellowish to reddish/orange bacteria mats. A complete photomosaic of the outer crater area was not completed on the cruise and thus observations of the outer crater were restricted to areas traversed by the ROV. As in the inner crater, several areas of decimeter-scale yellowish mounds were aligned in linear fashion suggesting control of fluid flow by crater faults (Figure S-1, movie S3). The surfaces of the mounds were covered with loose, flocculent, bacteria that were yellowish in color. Measured temperatures in these areas were typically 5-10$^o$ C above ambient temperature of 15$^o$ C.

**4.3 Bacterial mats**

Bacterial mats are common in both the main and inner crater of KeJ. They are found in a variety settings including rocky outcrops (Figure 6a), flat sedimented areas (Figure 6b) and focused fluid vents on the inner crater slopes. The majority of the mats in low temperature areas (<50$^o$ C) are yellowish orange in color with numerous small circular holes that appear to be places where diffuse flow is being discharged (Figure 6c). In higher temperature areas (>50$^o$ C) they are predominantly white in color and filamentous.

Genetic fingerprinting of two KeJ sample are compared by cluster analysis with other hydrothermal sites from a wide variety of geological/tectonic environments in figure 7. Three distinct groups were formed based on the DNA similarities. The most dissimilar microbial community shown, Lower Jet Vents (1997), was sampled directly after an eruptive event at Loihi Seamount off of Hawaii. This microbial mat was found to be dominated by a single phylotype (DNA similarities) most closely related to the *Epsilonproteobacteria*, *Nitratiruptor* and is hypothesized to have represented a bloom event. These organisms can be characterized by related isolates, which are all strict chemolithoautotrophs capable of respiratory nitrate reduction using hydrogen and forming $N_2$ as a metabolic product. The rest of Group I is comprised of more complex communities that all contain *Epsilonproteobacteria* that are phylogenetically similar and capable of hydrogen oxidation (e.g., *Nitratiruptor*, *Caminibacter*, *Nautilia*, *Thioreductor*, and/or *Lebetimonas*). Group II also contains more complex communities that cluster together by the presence of a second phylogenetically similar group of *Epsilonproteobacteria*; however, these are mostly sulfur-oxidizing types (e.g., *Sulfurimonas*, *Sulfurovum*, and/or *Sulfuricurvum*). Finally, samples in the third group (Group III) are clustered together by the presence of *Zetaproteobacteria*, which are known to use iron-oxidation and have been hypothesized as both ecosystem engineers and primary producers in these iron-rich ecosystems (Figure 7).

The mats found at Champagne Vent (KeJ inner crater) are represented within Group I and comprise a community dominated by *Epsilonproteobacteria*, most likely associated with hydrogen-oxidization. The mats found at the Fe-oxyhydroxide vent (southeast wall of inner crater) primarily represent the *Epsilonproteobacteria*, which are putative sulfur-oxidizers (Group II); however, this mat community was also found to contain some *Zetaproteobacteria* phylotypes (based on fragment-sizing identification), accounting for the resulting intermediate association between Group II and Group III (Figure 7). The comparison vent sites in figure 7, along with the timing of collection, represent a broad spectrum of hydrothermal vent habitats. The seamount sites along the Mariana Arc (Seamount X, Esmeralda Bank, NW Eifuku, Daikoku, NW Rota, E Diamante) represent a variety of venting geochemistries and the resulting communities are dispersed across the breadth of the T-RFLP dendrogram (Figure 7). The Loihi samples in Group III (Lohiau, Hiolo, Pohaku, Lower jet vents) were gathered from more diffuse venting sites that were high in ferrous iron (often up to nearly a mM concentrations). Samples from KeJ show affinities to community structures from several types of habitats, as would expected based on the observed variations in venting temperature and mineralization in the crater area.

**4.4 Gas Discharge in the Inner Crater**

Numerous streams of bubbles were detected in the inner crater by reflections in the water column data collected by the shipboard multibeam system (Figure 8). At least three large gas venting areas could be identified, with the most vigorous occurring near the Champagne and Shrimp vents (Figure 2). Samples of the gases at these vents were collected using titanium gas-tight bottles with an inverted funnel system (movie S4).

#### 4.4.1 Gas Compositions

Gases collected at both vent sites contain dominantly carbon dioxide (>92%) with minor amounts of methane and nitrogen (Table 3). Sulfur species ($H_2S$ or $SO_2$) were not analyzed but are assumed to constitute the components making up the difference between the analyzed gas species and the analytical totals (1.2-4.7%). Based on detection of $H_2S$ during analysis of the hydrocarbon components, it is suggested that this was the dominant sulfur species in the samples.

Gases at the Champagne vent were collected from two bubble streams; a strong one at the top of the mound (NA039-009) and a much weaker one on the side (NA039-010). Bubbles in the strong stream were translucent, whereas bubbles from the weak stream were clear. No significant difference in composition was found between the two streams (Table 3). A single gas sample collected at the Shrimp vent (NA039-091) was slightly richer in carbon dioxide (Table 3) and very similar in composition to gases collected from other submarine arc volcanoes in the western Pacific [*Lupton et al., 2008*].

#### 4.4.2 Gas Flux Measurements

Measurements of gas flux were carried out on the two bubble streams that were sampled and analyzed for gas composition at the Champagne vent and one bubble stream at the Shrimp vent (Table 4, movie S-5, methods S-1). Temperature was measured using a probe at the exit point of the bubble streams from the seafloor. The flux rates for the strong bubble stream at the top of the Champagne mound averaged 33 cc/s. Assuming that the gas was at the temperature measured at the discharge point (107$^{o}$ C) and that $CO_2$ was 93% of the gas, this stream was producing about

1.0 g of $CO_2$ per second or about 100 kg $CO_2$ per day (Table 4). A single discharge measurement at the weaker bubble stream on the side of the mound yielded a rate of 1.5 cc/s and $CO_2$ flux of 0.1 g/c and 6 kg/day based on a $CO_2$ content of 93% and temperature of 16$^o$ C. At Shrimp vent the average gas flux was 9.0 cc/s (Table 4). This yields a $CO_2$ flux of 0.4 g/s and 36 kg/day based on a $CO_2$ content of 96% and temperature of 28$^o$ C.

## 4.5 Hydrothermal Deposits

A wide variety of hydrothermally-derived or potentially altered deposits were observed and sampled in the inner crater of Kick'em Jenny (Figure 2). These include fine-grained silty-clayey sediment, dark-colored silty/sandy volcaniclastic sediment, indurated vent precipitates, sulphide-cemented volcanic breccia, Fe-oxyhydroxide chimneys, and bacterial mats.

### 4.5.1 Lithology/mineralogy of inner crater sediments

A distinctive feature of the inner crater is the widespread occurrence of bluish-gray, fine-grained silty/clayey sediment found in areas of active hydrothermal venting, often as low relief mounds (Figure 2). A darker, and generally more coarse-grained silty/sandy sediment, is dominant in areas with little or no obvious hydrothermal venting. Petrographic analysis reveals a similarity in components for both sediment types within the 500 to 63 micron (μm) size classes. Both consist of mafic crystals (amphibole and pyroxene), plagioclase, and dark scoria in roughly similar proportions, and are considered to be volcaniclastic fragments of KeJ lava and scoria formed by explosive disruption during submarine eruptions (Figure S-3).

Pyrite, anhydrite, and silica were identified by SEM energy dispersive x-ray spectroscopy from two of the silty/clayey samples (RB-03-03-18 and RB-03-03-31). Most of the pyrite was found in the 500-125 μm size range, whereas euhedral anhydrite crystals were mostly concentrated in the 250-125 μm fraction. In contrast, the silty/sandy sediment did not contain any individual pyrite or anhydrite grains, although massive pyrite and euhedral galena were identified as overgrowths on some primary igneous minerals.

XRD analyses allowed for a more complete characterization of sediment mineralogy, especially in the fine grain sizes (Table 5). Silty/clayey samples consist of a mixture of igneous minerals (plagioclase), clay minerals (smectite, illite, vermiculite, and illite/smectite (I/S) mixed layer), other alteration minerals (diopside, talc, quartz, and actinolite), sulfides (pyrite), and sulfates (magnesite). The clay fraction from the silty/clayey sediment was found to consist of iron- and Mg-rich clays as well as a Fe-oxyhydroxide phase and an unidentified iron silicate.

At the Champagne vent and to a lesser extent the Shrimp vent, discharge of fluid and gases was occurring from localized mounds of highly-indurated grayish brown sediment that was firm enough to be picked up the ROV (Figure 3a,b). This material differed from the generally softer silty/clayey and silty/sandy volcanic sediment of the inner crater and smelled strongly of sulfur when brought to the surface. XRD analyses indicate that the material contains a mixture of igneous minerals (plagioclase and pyroxene), minor talc and pyrite, and abundant nontronite, an Fe-rich smectite commonly associated with low temperature alteration of basaltic rocks (Table 5).

**4.5.2 Grain size of inner crater sediment**

Grain size analysis of the silty/clayey and silty/sandy volcanic sediment reveals distinct differences in size and sorting. The percentage of grains > 500 μm is greatest for the silty/sandy volcanic samples (10-17%) and lowest for the silty/clayey samples (0-6%). Because grains < 500 μm constitute a significant percentage of the samples, distributions of grains < 500 μm were determined with a high-resolution laser Mastersizer2000 and then mass adjusted to the total sample weight. Results support the observation that the silty/clayey sediment is significantly finer grained than the silty/sandy volcanic sediment (Figure 9). The majority of silty/clayey sediment is < 20 μm with a range in mean size of 8 – 29 μm and a range in mode of 8 – 19 μm (Figure 9). In contrast, silty/sandy sediment is bimodal with samples showing peaks at 18-30 μm and 180-300 μm. The percentage of clay-sized grains is greatest for the silty/clayey samples (6-19%) and smallest for the silty/sandy samples (~2%). In general, the silty/clayey samples are poorly sorted with fine skewness and a small percentage of grains ~200 μm, whereas the one silty/sandy sample is typically more poorly sorted.

**4.5.3 Geochemistry of inner crater sediments**

Major element compositions (Table 6) of the two types of sediment are plotted together with major element data of KeJ lava and scoria samples in Figure 10. The plots show that the silty/sandy sediments fall within the compositional fields for KeJ lava/scoria, but the silty/clayey sediments are offset significantly with respect to both the silty/sandy sediment and KeJ lava/scorias. In particular, the silty/clayey sediment is depleted in $Al_2O_3$, but enriched in MgO and $Fe_2O_3$* when compared with silty/sandy sediment and KeJ lava/scoria at similar $SiO_2$ contents (Figure 10). Geochemical mass balance calculations were carried out to evaluate whether the silty/clayey sediment was related to the silty/sandy sediment by alteration processes. Sample RB-03-03-18 was chosen as a representative silty clay and RB-03-03-28 was selected as primary silty/sandy volcanic sediment. Alteration clay mineral compositions were taken from the literature [*Cole, 1988; Turner et al., 1993; Severmann et al., 2004; Lackschewitz et al., 2004; Dekov et al., 2008a,b; Cuadros et al., 2008*] and the maximum pyrite component (2.3%) was calculated from XRF wt% sulfur data for RB-03-03-18 assuming all sulfur is present as pyrite. The best fit was achieved when silty/clayey sediment was modeled as 71% primary volcanic sediment, 4% I/S mixed layer clays, 3% smectite, 17% talc, 4% illite, and 1% pyrite (Appendix

Table S-1 and Figure S-6).

Trace element abundances (Table 7) of silty/clayey (bulk and clay size fraction) sediment relative to silty/sandy sediments are shown in Figure 11. For the purpose of this study, only samples with a basaltic composition are compared because the majority of samples are basaltic in composition and patterns of incompatible and compatible trace elements typically change during processes of magmatic evolution. Silty/clayey bulk and clay samples are enriched in Cu, As, Sb, Tl, and Bi by a factor ≥2 with slightly greater enrichments in the clay fraction than the respective bulk fraction (Figure 11).

#### 4.5.3.1 Sulphide-bearing volcanic breccia

Only one sample collected from the inner crater of KeJ showed significant development of sulphide mineralization (RB-03-08). This sample is a volcanic breccia consisting of a single large scoria block with other fragments of scoria, pumice, and lava cemented to the exterior by pyrite overgrowths (Figure 12). SEM imagery of the pyrite grains (Figure S-4) shows distinct crystal morphologies (bladed, blocky, equant, acicular and pelletal) indicative of different stages of pyrite growth from hydrothermal fluids with varying temperature and composition [*Murowchick and Barnes, 1987*].

#### 4.5.3.2 Geochemistry of sulphide-bearing volcanic breccia

Major oxide and trace element analyses were carried out on the precipitate-encrusted exterior (P) and fresh interior (WR) of the sulphide-bearing volcanic breccia [Tables 6 and 7]. The exterior sample is slightly depleted in major oxides except for a constant MgO value and significant enrichment in total FeO relative to the unaltered interior (Figure S-5). A majority of the trace elements are depleted in the exterior precipitates relative to the interior with the exception of Sc, Cr, and Ni. The enrichment in total Fe of RB-03-03-08P is most certainly due to the presence of pyrite overgrowths that cement lithic fragments to the original scoria and to the presence of Fe(oxy)-hydroxides. The composition of pyrite overgrowths was determined by electron microprobe. Figure S-4 shows the range in Fe wt% and S wt% of several pyrite aggregates that differ in crystal habit. The iron content in pyrite aggregates encompasses a significant range, from 44.8- 49.0 wt%. Sulfur content, on the other hand has a narrower range, from 52.1- 53.6 wt%. The higher values of iron are associated with pyrite aggregates with fewer crystal faces and, therefore, an indistinct crystal habit (Figure S-4).

### 4.5.4 Iron oxy-hydroxide chimneys

The mineralogy of the delicate chimneys located predominantly along the southeast wall of the inner crater (Figure 3c) consists largely of amorphous silica and ferrihydrite with lesser amounts of goethite and nontronite (Table 5). This is reflected strongly in the bulk major element composition of this material with a $SiO_2$ content of 48.53% and total iron value of 40.95 (Table 6).

## 5.0 Discussion

### 5.1 Gas Discharge

Hydrothermal venting at Kick'em Jenny includes both fluid and gas discharge at numerous locations in the inner crater. The gas is dominantly carbon dioxide with discharge rates as high as 100 kg/day from individual bubble streams. Gas flux measurements are relatively rare at submarine volcanoes and have relied on a combination of data sets such video imagery, compositional analyses of collected samples, and acoustic signals to infer discharge rates [ e.g. Lupton et al., 2006; Dziak et al., 2012], We anticipate that our flux numbers will be useful in constraining a future analysis of the total gas flux from the KEJ crater. Ongoing work is attempting to quantify the total number of bubble streams (likely hundreds) from the crater using multibeam data and then to assign some likely gas flux based on the acoustic strength of streams and the individual measurements presented in this paper.

Dissolution of $CO_2$ after venting has likely lead to decreases in crater water pH as observed at other shallow water volcanic centers with impacts on marine fauna [*Hall-Spencer et al., 2008; Tunnicliffe et al., 2009; Carey et al., 2013; Camilli et al., 2015*]. Several pH measurements were collected around the Champagne and Shrimp vents using a ROV-deployed pH meter. Values as low as 4.0 were recorded when the probe was located in close proximity to the vents (few centimeters), but even at distances up to a few meters the pH values were significantly less than ambient seawater.

The helium isotopic ratio of venting gases at KeJ averaged 6.73 (Table 3). This falls in the range of ~5-7 for arc volcanoes defined by *Sano and Marty* [1995] suggesting a contribution of slab-derived helium to the KeJ magmatic system. A strong slab/sediment contribution to volcanoes in the southern Lesser Antilles has also been indicated based on elevated lead and strontium isotopic ratios [*White and Dupre, 1986*] and extremely high values of U-excess ($^{238}U/^{232}Th$) in KeJ lavas [*Gill and Williams, 1990*].

### 5.2 Origin of silty/clayey crater sediment

We suggest that the distinctive silty/clayey sediment found in KeJ's inner crater is the result of hydrothermal alteration of primary silty/sandy volcanic sediment produced during explosive eruptions of the volcano [e.g. *Hocking et al., 2010*]. Alteration of basalt and dacite to clay minerals during hydrothermal circulation is well known [*Sturz et al., 1998; Zierenberg et al., 1995; Lackeschwitz et al., 2004*], but alteration of volcanic sediments to clay minerals is still an ongoing area of research [*Severmann et al., 2004; Lackschewitz et al., 2004; Dekov et al., 2008a,b; Hocking et al., 2010*]. The presence of illite and I/S mixed layer clays in KeJ silty/clay and the geochemical mass balance calculations supports the interpretation of a hydrothermal alteration origin for the majority of the clay fraction. Alteration of the volcaniclastic sediment in the inner crater has thus resulted in the formation of a sediment layer with reduced permeability relative to the primary silty/sandy tephra. Geochemical data indicate that this layer constitutes a significant sink for Mg from circulating fluids and a zone of enrichment of fluid-derived metals such as Cu, As, and Sb. The results suggest that hydrothermally altered tephra may play an important role in the net geochemical fluxes in shallow arc venting systems such as KeJ.

### 5.3 Formation of sulphide volcanic breccia

Surficial sulphide mineralization occurs only rarely in areas of highest fluid temperature and produces localized cemented volcanic breccia (Figure 12). Relative to the host basaltic scoria, the sulphide-mineralized exterior is depleted in virtually all trace elements except Cr and Ni. The relative enrichment in Cr and Ni in the altered exterior is most likely due to Cr and Ni contents in the individual fragments cemented by pyrite overgrowths. A wide range in Cr and Ni content is typical of KeJ lavas/scorias and is, therefore, more likely reflective of lithological heterogeneity rather than hydrothermal processes. Relative depletions in trace elements, however, especially as they relate to pyrite overgrowths, are probably associated with hydrothermal processes. A lack of enrichment in Cu and As, in particular, is noteworthy because both elements are known to substitute for Fe during pyrite formation [*Deditius et al., 2009*]. *Deditius et al. [2009]* found that pyrite from high-sulfidation deposits consist of distinct growth zones enriched in either Cu or As. Phase separation and fluid mixing are two mechanisms that would cause abrupt changes in the composition of a hydrothermal fluid and result in depletions/enrichments of Cu and As [*Deditius et al., 2009*]. Both elements are strongly partitioned into the vapor phase during phase separation of hydrothermal fluids [ *Heinrich et al., 1999; Pokrovski et al., 2002*]. In the case of pyrite overgrowths on the hydrothermal breccia in this study, the lack of Cu or As enrichment suggests that the hydrothermal fluid from which the pyrite precipitated may have been a barren, brine-rich fluid produced during phase separation at depth beneath the inner crater of KeJ.

## 5.4 Model for the hydrothermal system at Kick'em Jenny

### 5.4.1 Evidence for phase separation of hydrothermal fluids

Previous studies of distal vent fluids from Kick'em Jenny volcano found that bottom seawater samples were depleted in Mg and Cl relative to ambient seawater but enriched in Zn, Cu, Ni, and As [*Koschinsky et al., 2007*]. This geochemical association was interpreted by *Koschinsky et al.* (2007) to represent the condensed vapor phase of a phase-separated hydrothermal fluid with initial temperatures up to 280°C. Our new results from the inner crater of KeJ provide strong support for the occurrence of phase-separation in the KeJ hydrothermal system. First, evidence for vapor phase venting is suggested by geochemical analyses of KeJ sediments from the inner crater. Silty/clayey sediments were found to be enriched in Cu, As, and Sb relative to silty/sandy volcanic sediment (Figure 11), in accord with studies that cite the strong partitioning of these elements into the vapor phase during phase separation [*Heinrich et al., 1999; Pokrovski et al., 2002, 2008; Deditius et al., 2009*]. Based on these studies, the most likely reason for the relative enrichment of these elements is the high temperature alteration of silty/sandy sediment to silty/clayey sediment by a condensed vapor-separated fluid. In locations where pyrite precipitation is forming hydrothermal breccias (Figure 12), the altered pyrite exterior is relatively depleted in trace elements, most notably Cu, As, and Sb, suggesting deposition from a relatively dense brine that had lost significant metals through deposition sub-surface. Brines can have excess iron available for barren pyrite deposition if an additional source of sulfur is added through mixing with a condensed vapor phase or seawater [*Seo et al., 2009*].

Second, the unusual downslope fluid flow patterns in the inner crater (Figures 2,3) indicate that some of the venting fluids, especially around the margins of the inner crater are denser, and thus likely more saline, than ambient seawater. Such fluids may therefore represent brines that were generated by phase separation of hydrothermal fluids beneath the floor of the inner crater. Density measurements of fluids collected in the inner crater support the formation of denser vent fluids relative to ambient seawater (Figure 5), although the differences are small and likely reflect extensive mixing prior to discharge. We note that the venting of high-salinity brines is somewhat discordant with observations and models from deeper and higher-temperature systems along mid-ocean ridges where brines are believed to stall in the subsurface. In the case of KeJ, the possibility that phase separation occurs relatively near the seafloor may facilitate the venting of these brines. Increases in fluid density may also be the result of high levels of dissolved $CO_2$ as proposed at some other shallow arc volcanoes [*Carey et al., 2013; Camilli et al. 2015*].

Suitable conditions for phase separation are predicted to occur at Kick'em Jenny due to the relatively shallow depth of the inner crater (~250 mbsl) and maximum temperatures measured at the venting sites (up to 270°C in 2003 at 10 cm below sediment surface). Based on the seawater boiling curve developed by *Bischoff and Rosenbauer* [1987] subcritical vapor generation would take place at ~220°C.

#### 5.4.2 Mineralization

Surface mineralization within the inner crater of Kick'em Jenny is characterized by a dominance of yellowish-orange Fe(oxy)-hydroxides mats/mounds and a lack of sulphide chimneys (movie S6). The absence of sulphide chimneys is not unusual in shallow water hydrothermal systems. Rather than being enriched in Fe-sulfides, many shallow water hydrothermal systems exhibit amorphous Fe-oxyhydroxides, crystalline FeOOH, or iron silicate minerals, especially smectite on or near the seabed [*Hein et al., 2008*]. Removal of sulfides from hydrothermal fluids via precipitation of metal sulfides in the sub-seafloor has been suggested as an important final step in the formation of Fe-oxyhydroxide deposits by a number of models [e.g. *Pichler & Veizer, 1999*].

Fe-oxyhydroxides at many submarine volcanoes are associated with iron oxidizing bacteria (FeOB) that are likely to have played a significant role in the precipitation of iron-bearing phases, referred to as bacteriogenic iron oxyhydroxides (BIOS) [*Kari et al., 1988; Emerson and Moyer, 2002, 2010; Emerson et al., 2010; Ferris, 2005*]. At Loihi seamount off of Hawaii, 60% of the iron oxide deposition has been attributed to microbial activity [*Emerson and Moyer, 2002*]. The extensive iron oxide deposition at KeJ bears many similarities to the observed deposits at Loihi, such as the presence of both extensive mats in areas of low temperature diffuse flow (10-30$^{o}$ C) and small chimney-like structures at higher temperature (50$^{o}$ C) [*Emerson et al., 2010*]. Fluids venting at Loihi are rich in $CO_2$ and acidic compared with other submarine hydrothermal systems [*Kari et al., 1988*]. pH is a critical parameter in controlling the kinetics of $Fe^{+2}$ oxidation, and under low pH conditions microbial-activated precipitation of BIOS is enhanced due to slower rates of abiotic oxidation [*Ferris, 2005*]. Measurements of dissolved oxygen in the crater at KeJ near the Champagne vent (Figure 5) show that values are of the order of 150 uM and thus not a limiting factor for abiotic oxidation. At KeJ the active venting of $CO_2$ and low pH measurements around the inner crater vents suggest that, like Loihi, conditions are favorable for microbrially-dominated precipitation of BIOS. The bacterial community at KeJ shows evidence of both *Zetaproteobacteria* (Fe-oxidizers) and *Epsilonproteobacteria* (sulfur oxidizers) in accord with the observed spectrum of fluid discharges from low temperature Fe-oxyhydroxide vents ($<50^{o}$ C) to higher temperature ($\sim180^{o}$ C) vents with sulphide-bearing breccias.

Most metals dissolved in hydrothermal fluids at KeJ were suggested to have been deposited sub-seafloor during phase separation based on the composition of hydrothermal fluids detected in the water column [*Koschinsky et al., 2007*]. The implication of this is that there is potentially significant subsurface sulphide mineralization occurring beneath the crater floor of Kick'em Jenny at the present time. This system may be analogous to the well-studied mineralized zones of Palinuro submarine volcano in the Aeolian arc [*Petersen et al., 2008; Monecke et al., 2009*]. At this site there are abundant Fe-oxyhydroxide chimneys and bacterial mats associated with relatively low temperature venting [*Carey et al., 2012*]. These chimneys are very similar in appearance to those found along the SE inner crater wall of KeJ (Figure 3c). Shallow drilling on the west end of Palinuro revealed thick deposits of massive sulphide deposits lying only tens of centimeters below a thin covering of fine-grained sediment [*Petersen et al., 2008*]. Similar sulphide deposits may lie beneath the KeJ crater although repeated disruption by frequent eruptions during the recent past would likely hinder their preservation. The crater would certainly be an interesting target for the type of shallow drilling carried out at Palinuro in order to further explore the mineralization occurring at KeJ.

Many features of the KeJ hydrothermal system also show significant similarities to the young Nafanua cone in the crater of Vailulu'u seamount in the western Pacific [*Staudigel et al*, *2006*]. These include evidence for relatively shallow water phase separation of hydrothermal fluids, dominance of Fe-oxyhydroxide deposition with associated bacterial mats, active $CO_2$ discharge, and frequent eruptive activity.

The results of our study confirm the interesting complexities of shallow water hydrothermal systems in shallow submarine volcanoes. These environments are characterized by compositionally diverse fluid and gas discharges, are susceptible to phase separation of fluids, and occur within craters that are often filled with volcaniclastic sediment. Such conditions can lead to interesting fluid flow patterns, induced by phase separation, that have implications for both the nature and location of mineralization and the spatial distribution of associated ecosystems.

## 6.0 Conclusions

Hydrothermal venting and mineralization at Kick'em Jenny submarine volcano in the West Indies has been investigated by remotely operated vehicle (ROV) explorations of the crater and surrounding slopes. Clear fluids up to 180$^{o}$ C and gases are being discharged through fine- and coarse-grained volcaniclastic sediment of basalt/basaltic andesite composition that has been produced by repeated shallow water explosive eruptions. This sediment has been partially altered to smectite, illite and Fe-oxyhydroxides by circulating hydrothermal fluids. Gases collected at two sites in the crater were relatively homogenous and dominated by $CO_2$ (>92%) with minor amounts of $H_2S$. Measured flux rates of individual bubble streams varied from 10 to 100 kg of $CO_2$/day.  Rare sulphide mineralization occurs as barren pyrite-cemented breccias in areas of highest temperature fluid discharge focused primarily in a small 70 x 110 meter depression within the volcano's main crater at a depth of 265 meters. The most common mineralization is the extensive development of mats, mounds, and small spires of fragile Fe-oxyhydroxides in areas of diffuse and relatively low temperature fluid discharge (~30$^{o}$>ambient). Deposition of this material is likely to be facilitated by Fe-oxidizing bacteria (*Zetaproteobacteria)* found in these areas. High-resolution photomosaics of the crater reveal distinctive downslope flow patterns of hydrothermal fluids that resemble braided streams. We propose that production of dense fluids was likely caused by subcritical phase separation at depth beneath the crater with subsequent venting of both condensed vapor and brine components that were remixed with circulating seawater as they moved through the porous volcaniclastic sediment. Support for the phase separation model includes 1) the P/T conditions in the crater area relative to the seawater boiling curve, 2) enrichment in As and Cu (strongly partitioned into a vapor phase) in hydrothermally-altered crater sediment, 3) high-precision measurement of fluid densities collected at different locations in the crater and 4) discovery of chloride-depleted seawater just outside of the crater by previous water column studies. Based on a comparison with other shallow water volcanic arc hydrothermal systems with similar development of extensive surficial Fe-oxyhydroxides there is the potential that significant massive sulphide deposition may be occurring at shallow levels within the volcaniclastic sediment pile currently filling the crater. Such deposits are, however, likely to be quite ephemeral due to the highly active nature of the volcano with eruptions occurring at least one per decade.

**7.0 Acknowledgements**

We thank the captain, crew, and expedition team of E/V *Nautilus* for their excellent work during cruises NA039 and NA054. The Ocean Exploration Trust (OET), National Oceanographic and Atmospheric Administration (NOAA), and the National Geographic Society provided support for the cruises. The Seismic Research Centre of the University of the West Indies in Trinidad contributed invaluable assistance during the cruises and the Government of Grenada is gratefully acknowledged for permission to operate in their territorial waters.

Ian Vaughn kindly provided images of bubble streams from KeJ crater derived from shipboard multibeam data. Scott Wankel and Ana Michel (both at WHOI) are thanked for sharing fluid samples collected during cruise NA054 that were used for density measurement. Art Spivack provided insightful discussions about phase separation processes in hydrothermal systems. Rich

Bell is thanked for his help in collating the oxygen sensor data. Four reviewers provided useful comments that led to improvements in the manuscript. All numerical data is shown in figures or presented within tables in the text or as supporting information.

**References**

Baker, E. T., R. W. Embley, S. L. Walker, J. A. Resing, C. E. J. de Ronde, G. J. Massoth, and K.-I. Nakamura (2008), Hydrothermal activity and volcano distributions along the Mariana Arc, *Jour. Geophys. Res., 113,* B08S09, doi:10.1029/2007JB005423.

Bischoff, J. L. and R. J. Rosenbauer (1987), Phase separation in seafloor geothermal systems: An experimental study of the effects on metal transport, *Amer. Jour. Sci., 287*, 953-978.

Bouysse, P., D. Westercamp, and P. Andreieff (1990), The Lesser Antilles Island arc, *Proceedings of the Ocean Drilling Program, Scientific Results, 110*, 29-44.

Camilli, R., P. Nomikou, J. Escartin, P. Ridao, A. Mallios, S. Kilias, A. Argyraki, M.Andreani, V. Ballu, R. Campos, C. Deplus, T. Gabsi., R. Garcia, N. Gracias, N. Hurtos, L. Magi, C. Mevel, M. Moreira, N. Palomeras, O. Pot, D. Ribas, L. Ruzie, and D. Sakellariou (2015), The Kallisti Limnes, carbon dioxide-accumulating subsea pools. *Nature Scientific Reports*, DOI: 10.1038/srep12152.

Carey, S., K.L.C., Bell, , M. Rosi, M. Marani, P. Nomiku, S. Walker, K. Faure, K., and J. Kelly (2012), Submarine volcanoes of the Aeolian Arc, Tyrrhenian Sea. *Oceanography*, 25(1), 32-33.

Carey, S., P. Nomikou, K. Croff Bell, M. Lilley, J. Lupton, C. Roman, E. Stathopoulou, K. Bejelou, and R. Ballard (2013), $CO_2$ degassing from hydrothermal vents at Kolumbo submarine volcano, Greece, and the accumulation of acidic crater water,. *Geology, 41,* 1035–1038.

Carey, S., K.L.C. Bell, R.D. Ballard, C. Roman, F. Dondin, P. Miloslavich, J. Gobin, B. Seibel, C. Smart, S. Fuller, N. Siu, P. Connally, R. Blake, K. Wishner, and B. Phillips (2014a), Fluid/gas venting and biological communities at Kick'em Jenny submarine volcano, Grenada (West Indies), *Oceanography, 27(1)*, 38-41.

Carey, S., R.D. Ballard, K.L.C. Bell, R. Bell, P. Connally, F. Dondin, S. Fuller, J. Gobin, P. Miloslavich, B. Phillips, C. Roman, B. Seibel, N. Siu, and C. Smart (2014b), Cold seeps associated with a submarine debris avalanche deposit at Kick'em Jenny submarine volcano, Grenada (West Indies), *Deep-Sea Research I, 93(1)*, 156-160.

Carey, S., Bell, K.L.C., Roman, C., Dondin, F., Robertson, R., Gobin, J., Wankel, S., Michel, A., Amon, D., Marsh, L., Smart, C., Vaughn, I., Ball, B., Rodrigue, K., Haldeman, M., George, A., and R.D. Ballard (2015), Exploring Kick'em Jenny Submarine Volcano and the Barbados Cold Seep Province, Southern Lesser Antilles, *Oceanography, 28(1)*, 38-39.

Cole, T. (1988), The nature and origin of smectite in the Atlantis II Deep, Red Sea, *Can. Mineral.*, 26, 755-763.

Cuadros, J., V. M. Dekov, and S. Fiore (2008), Crystal chemistry of the mixed-layer sequence talc-talc-smectite-smectite from submarine hydrothermal vents, *Amer. Mineral., 93*, 1338-1348.

Davis, R. and C. Moyer (2008), Extreme spatial and temporal variability of hydrothermal microbial mat communities along the Mariana Island Arc and southern Mariana back-arc system, Jour. Geophys. Res., 113, B08S15, doi:10.1029/2007JB005413.

Deditius, A. P., S. Utsunomiya, R. C. Ewing, S. L. Chryssoulis, D. Venter, and S. E. Kesler (2009), Decoupled geochemical behavior of As and Cu in hydrothermal systems, *Geology, 37(8)*, 707-710.

Dekov, V. M., J. Cuadros, W. C. Shanks and R. A. Koski (2008a), Deposition of talc—kerolite-smectite-—smectite at seafloor hydrothermal vent fields: Evidence from mineralogical, geochemical and oxygen isotope studies, *Chem. Geol., 247*, 171-194.

Dekov, V. M., J. Scholten, C.D. Garbe-Schonberg, R. Botz, J. Cuadros, M. Schmidt and P. Stoffers (2008b), Hydrothermal sediment alteration at a seafloor vent field: Grimsey Graben, Tjörnes Fracture Zone, north of Iceland. *Jour. Geophys. Res., 113(B11101),* 1-20.

de Ronde, C. E. J., G. J. Massoth, E. T. Baker, and J. E. Lupton (2003), Submarine hydrothermal venting related to volcanic arcs, *Soc. Econ. Geol. Spec. Publ., 10*, 91–110.

de Ronde, C. E. J., E. T. Baker, G. J. Massoth, J. E. Lupton, I. C. Wright, R. J. Sparks, S. C. Bannister et al. (2007), Submarine hydrothermal activity along the mid-Kermadec arc, New Zealand: Largescale effects on venting, *Geochem. Geophys. Geosyst., 8*, Q07007, doi:10.1029/2006GC001495.

Devas, R.P. (1974), History of the island of Grenada. *Carenage Press*, St. George’s, Grenada, 1498-1796.

Devine, J. D. (1995), Petrogenesis of the basalt-andesite-dacite association of Grenada, Lesser Antilles island arc, revisited, *Jour. Volcanol. Geotherm. Res., 69*, 1-33.

Devine, J. D. and H. Sigurdsson (1995), Petrology and eruption styles of Kick 'em Jenny submarine volcano, Lesser Antilles island arc, *Jour. Volcanol. Geotherm. Res., 69*, 35-58.

Dondin, F., J.F. Lebrun, K. Kelfoun, N. Fournier, and A. Randrianasolo (2012), Sector collapse at Kick’em Jenny submarine volcano (Lesser Antilles): numerical simulation and landslide behavior, *Bull. Volcanol., 74*, 595-607.

Drummond, S. E. and H. Ohmoto (1985), Chemical Evolution and Mineral Deposition in Boiling Hydrothermal Systems, *Econ. Geol., 80*, 126-147.

Dziak, R., E. Baker, A. Shaw, D. Bohnenstiehl, W. Chadwick, W., J. Haxel, H. Matsumoto, S. Walker (2012), Flux measurements of explosive degassing using a yearlong hydroacoustic record at an erupting submarine volcano, *Geochem. Geophys. Geosyst.*, 13, Q0AF07, doi:10.1029/2012GC004211.

Emerson, D. and C. Moyer (2002), Neutrophilic Fe-Oxidizing Bacteria Are Abundant at the Loihi Seamount Hydrothermal Vents and Play a Major Role in Fe Oxide Deposition, *App. Environ. Microbio., 68(6)*, 3085-3093.

Emerson, D. and C. Moyer (2010), Microbiology of Seamounts, *Oceanography, 23(1)*, 148-163.

Emerson, D., D. Fleming, and J. McBeth (2010), Iron-oxidizing bacteria: an environmental and genomic perspective, *Annu. Rev. Microbiol.*, *64*, 561-583.

Edmond, J., G. Massoth, and M. Lilley (1992), Submersible-deployed samplers for axial vent waters. *Ridge Events 3 (1)* 23-24.

Edwards, K.J., W. Bach and T.M. McCollom (2005). Geomicrobiology in oceanography: microbe-mineral interactions at and below the seafloor. *Trends Microbiol. 13*, 449–56.

Ferris, F.G. (2005), Biogeochemical Properties of Bacteriogenic Iron Oxides, *Geomicrobiology Journal*, *22:3-4*, 79-85.

Folk, R.L. (1968), Petrology of Sedimentary Rocks. Hemphill's, Austin, Texas, 170 pp.

Gill, J.B., and R. Williams (1990), Th isotope and U-series studies of subduction related volcanic rocks. *Geochim. Cosmochim Acta*, 54, 1427-42.

Hall-Spencer, J., R. Rodolfo-Metalpa, S. Martin, E. Ransome, M. Fine, S. Turner, S. Rowley, D. Tedesco and M. Buia ( 2008), Volcanic carbon dioxide vents show ecosystem effects of ocean acidification, *Nature*, *454*, 96-99.

Hannington, M.D., C.E.J. de Ronde, and S. Petersen (2005), Sea-floor tectonics and submarine hydrothermal systems. *Econ. Geol. 100th Anniversary Volume*, 111-141.

Hein, J. R., D. A. Clague, R. Koski, R. Embley and R. Dunham (2008), Metalliferous sediment and a silica-hematite deposit within the Blanco Fracture Zone, Northeast Pacific, *Mar. Geores. Geotech., 26*, 317-339.

Heinrich, C. A., D. Gunther, A. Audetat, T. Ulrich, and R. Frischknecht (1999), Metal fractionation between magmatic brine and vapor, determined by microanalysis of fluid inclusions. *Geology*, *27(8)*, 755-758.

Hocking, M. W. A., M. D. Hannington, J. Percival, P. Stoffers, U. Schwartz-Schampera and C.E.J deRonde (2010), Clay alteration of volcaniclastic material in a submarine geothermal system, Bay of Plenty, New Zealand, *Jour. Volcanol. Geotherm. Res., 191,* 180-192.

Kari, D., G. McMurtry, A. Malahoff, and M. Garcia (1988), Loihi Seamount, Hawaii: a mid-plate volcano with a distinctive hydrothermal system, *Nature*, *335*, 532-535.

Kelley, K. A., T. Plank, J. Ludden and H. Staudigel (2003), Composition of altered oceanic crust at ODP Sites 801 and 1149, *Geochem. Geophys. Geosys. G3, 4(6),* 1-21.

Koschinsky, A., R. Seifert, A. Knappe, K. Schmidt, and P. Halback (2007), Hydrothermal fluid emanations from the submarine Kick 'em Jenny volcano, Lesser Antilles island arc, *Mar. Geol., 244*, 129-141.

Lackschiewitz, K. S., C. W. Devey, P. Stoffers, R. Botz, A. Eisenhauer, M. Kummetz, M. Schmidt and A. Singer (2004), Mineralogical, geochemical and isotopic characteristics of hydrothermal alteration processes in the active, submarine, felsic-hosted PACMANUS field, Manus Basin, Papua New Guinea, *Geochim. Cosmochim. Acta, 68(21),* 4405-4427.

Lindsay, J., J.B. Shepherd and D. Wilson (2005), Volcanic and scientific activity at Kick’em Jenny submarine volcano 2001-2002: implications for volcanic hazards in the southern Grenadines, Lesser Antilles, *Nat. Hazard, 34,* 1-24.

Lupton, J., D. Butterfield, M. Lilley, L. Evans, K. Nakamura, W. Chadwick, J. Resing et al.

(2006), Submarine venting of liquid carbon dioxide on a Mariana Arc volcano, *Geochem. Geophys. Geosyst.*, *7,* Q08007, doi:10.1029/2005GC001152.

Lupton, J., M. Lilley, D. Butterfield, L. Evans, R. Embley, G. Massoth, B. Christenson, K. Nakamura, and M. Schmidt (2008), Venting of a separate CO2-rich gas phase from submarine arc volcanoes: examples from the Mariana and Tonga-Kermadec arcs, *Jour. Geophys. Res.*, *113*, B08S12, doi:10.1029/2007JB005467.

Monecke, T., S., Petersen, K. Lackschewitz, M. Hugler, M. Hannington, and J. Gemmel (2009), Shallow submarine hydrothermal systems in the Aeolian volcanic arc, Italy, *EOS, 90(13)*, 110-111.

Murowchick, J. B. and H. L. Barnes (1987), Effects of temperature and degree of supersaturation on pyrite morphology, *Amer. Mineral.*, *72,* 1241-1250.

Nakagawa, S., Takai, K., Inagaki, R., Chiba, H., Ishibashi, J., Kataoka, S., Hirayama, H., Nunoura, T., Horikoshi, K. and Y. Sako (2005), Variability in microbial community and venting chemistry in a sediment-hosted backarc hydrothermal system: Impacts of subseafloor phase separation, *FEMS Microbial. Ecol., 54, 141-155.*

Olu, Karine, S. Lance, M. Sibuet, P. Henry, A. Fiala-Médioni, and A. Dinet (1997), Cold seep communities as indicators of fluid expulsion patterns through mud volcanoes seaward of the Barbados accretionary prism" *Deep Sea Research Part I: Oceanographic Research Papers,* 44, ( 5), 811-841.

Petersen, S., T. Monecke, N. Augustin, A.A. De Benedetti, A. Esposito, A. Gärtner, A. Gardeler, J.B. Gemmell, H. Gibson, G. He, M. Hügler, A. Kayser, R. Kleeberg, J. Küver, N. Kummer, K. Lackschewitz, F. Lappe, K.M. Perrin, M. Peters, R. Sharpe, K. Simpson, D. Smith, and B. Wan (2008), Drilling submarine hydrothermal systems in the Tyrrhenian Sea, Italy, *InterRidge News, 17*, 21-23.

Pichler, T. and J. Veizer (1999), Precipitation of Fe(III) oxyhydroxide deposits from shallow-water hydrothermal fluids in Tutum Bay, Ambitle Island, Papua New Guinea, *Chem. Geol., 162*, 15-31.

Pokrovski, G. S., A. Y. Borisova, and J.C. Harrichoury (2008), The effect of sulfur on vapor-liquid fractionation of metals in hydrothermal systems, *Earth Planet. Sci. Lett., 266,* 345-362.

Pokrovski, G. S., I. V. Zakirov, J. Roux, D. Testemale, J.L. Hazemann, A. Yu Bychkov, and G. V. Golikova (2002), Experimental study of arsenic speciation in vapor phase to 500°C: Implications for As transport and fractionation in low-density crustal fluids and volcanic gases, *Geochim. Cosmochim. Acta, 66(19),* 3453-3480.

Resing, J. A., E. T. Baker, J. E. Lupton, S. L. Walker, D. A. Butterfield, G. J. Massoth, and K. Nakamura (2009), Chemistry of hydrothermal plumes above submarine volcanoes of the Mariana Arc, *Geochem. Geophys. Geosyst., 10*, Q02009, doi:10.1029/2008GC002141.

Roman, C., G. Inglis, I. Vaughn, C. Smart, D. Dansereau, D. Bongiorno, M. Johnson-Roberson, and M. Bryson (2013), New tools and methods for precision seafloor mapping, *Oceanography, 26(1),* 10–15,

Sano, Y., and B. Marty (1995), Origin of carbon in fumarolic gas from island arcs, *Chem. Geol., 119*, 265 – 274, doi:10.1016/0009-2541(94)00097-R.

Seo, J. H., M. Guillong, and C. Heinrich (2009), The role of sulfur in the formation of magmatic-hydrothermal copper-gold deposits, *Earth Planet. Sci. Lett., 282,* 323-328.

Severmann, S., R. A. Millis, M. Palmer, and A. Fallick (2004), The origin of clay minerals in active and relict hydrothermal deposits, *Geochim. Cosmochim. Acta, 68(1),* 73-88.

Shepherd, J.B. and G.R. Robson (1967), The source of the T-phase recorded in the Eastern Caribbean on October 24, 1965, *Bull. Seismol. Soc. Amer., 57*, 227-234.

Sigurdsson, H. and J. B. Shepherd (1974), Amphibole-bearing basalts, from the submarine volcano Kick 'em Jenny in the Lesser Antilles arc, *Bull. Volcanol.*, *28*, 891-910.

Sigurdsson, H. and S. Carey (2003), NOAA Cruise Report R/V Ronald Brown RB-03-03. 10 p.

Sigurdsson, H., S. Carey, and D. Wilson (2006), *Debris avalanche formation at Kick'em Jenny submarine volcano* (p. 66). World Scientific, Hackensack, NJ.

Staudigel, H., S. Hart, A. Pile, B. Bailey, E. Baker, S. Brooke, D. Connelly, L. Hauke, C. German, I. Hudson, D. Jones, A. Koppers, J. Konter, R. Lee, T. Pietsch, B. Tebo, A. Templeton, R. Zierenberg, and C. Young (2006), Vailulu'u Seamount, Samoa: Life and death on an active submarine volcano, *PNAS, 103 (17)*, 6448-6453, doi/10.1703/pnas.0600830103.

Sturz, A., M. Itoh, and S. Smith (1998), Mineralogy and chemical composition of clay minerals, Tag hydrothermal mound, *Proc. Ocean Drilling Program Sci. Res.*, *158*, 277-284.

Tunnicliffe, V., K. Davies, D. Butterfield, R. Embley, J. Rose, and W. Chadwick (2009), Survival of mussels in extremely acidic waters on a submarine volcano, *Nature Geoscience*, *2*, 344-348.

Turner, R. J. W., D. E. Ames, J. M. Franklin, W. D. Goodfellow, C. H. B. Leitch, and T. Höy (1993), Character of active hydrothermal mounds and nearby altered hemipelagic sediments in the hydrothermal areas of Middle Valley, Northern Juan de Fuca ridge: data on shallow cores*, *Can. Mineral.*, *31*, 973-995.

Turner, S., C. Hawkesworth, P. van Calsteren, E. Heath, R. Macdonald, R. and S. Black (1996), U-series isotopes and destructive plate margin magma genesis in the Lesser Antilles. *Earth and Planet. Sci. Lett.*, 142, 191-207.

Von Damm, K. (1990), Seafloor hydrothermal activity: black smoker chemistry and chimneys. *Annu. Rev. Earth Planet. Sci.*, 18, 173-204.

Westbrook, G. K. (1982), The Barbados Ridge Complex: tectonics of a mature fore-arc system. In Leggett, J. K. (Ed.), *Trench-Forearc Geology*, *Geol. Soc. Spec. Publ. London*, 10, 275-280.

Westbrook, G.K. and M. Smith (1983), Long decollements and mud volcanoes: Evidence from the Barbados Ridge Complex for the role of high pore-fluid pressure in the development of an accretionary complex. *Geology*, 11, 279-283.

White, W. and B. Dupre (1986), Sediment subduction and magma genesis in the Lesser Antilles: isotopic and trace element constraints. *Jour. Geophys. Res*., 91, 5927-5941.

Zierenberg, R. A., P. Schiffman, I. R. Jonasson, R. Tosdal, W. Pickthorn, and J. McClain (1995), Alteration of basalt hyaloclastite at the off-axis Sea Cliff hydrothermal field, Gorda Ridge, *Chem. Geol., 126*, 77-99.

**Figure Captions**

Figure 1. Map showing the location of Kick'em Jenny submarine volcano off the coast of Grenada in the West Indies with shaded multibeam bathymetry collected during cruise NA-039. Inset map shows the Lesser Antilles island arc and location of the study area (red rectangle).

Figure 2. (left ) Multibeam bathymetric map of Kick'em Jenny submarine volcano from a 2013 survey on cruise NA039. Red rectangular box shows the high-resolution photomosaic area presented to the right. Depth contours in meters. The location of the most active gas discharging vents (Champagne and Shrimp) are marked by red stars. Note the pattern of fluid flow down the margins of the inner crater towards the relatively flat floor. A separate high resolution file of the photomosaic in available in the supplemental material (Figure S-1).

Figure 3. ROV images of a) Shrimp vent showing multiple bubble streams and white bacterial mats, b) Champagne vent with vigorous central bubble stream, c) fragile Fe-oxyhydroxide vents, and d) lumpy diffuse flow vents with abundant bacterial mats.

Figure 4. ROV images of a) bacterial mats colonizing fluid flow from the base of lava scree on east wall of inner crater and b) bacterial mats on the steeply sloping exposure of the Shrimp vent area. See Figure 3 for location.

Figure 5. CTD and oxygen profile in the crater of Kick’em Jenny over the Champagne vent. Salinities of fluid samples (stars) taken at various locations in the crater have been calculated based on measured fluid densities (Table 4). Vent samples were collected directly where fluids were discharged on the seafloor and Niskin samples were collected on the Hercules ROV at least 2 meters from the vent samples.

Figure 6. ROV images of a) bacterial mat filling in coarse lava breccia, b) push core being taken in thick bacterial mat on margin of inner crater, c) close-up of bacterial mat in b showing numerous small holes that likely act as fluid escape points, and d) white bacterial mats colonizing the area around the Shrimp vents.

Figure 7. T-RFLP fingerprinting of microbial mat communities from Kick’em Jenny hydrothermal vents in comparison with selected sites along the Mariana Arc as well as three other active submarine volcanoes from the Pacific Ocean (Loihi, Axial Seamount, and West Mata). Scale bar is Pearson product moment correlation r-value X 100. Numbers at nodes are cophenetic correlation values.

Figure 8. 3D multibeam bathymetry of Kick'em Jenny crater area showing bubbles emanating from the inner crater. Bathymetry color coded by depth (see scale in upper right hand corner).

Figure 9. Grain size distributions of a) silty/clayey sediment (18,31,40,41) and hemipelagic carbonate sediment (67) and b) silty/sandy volcanic sediment (28,32). Frequency curves based on Mastersizer2000 measurements.

Figure 10. Major oxide composition of silty/clayey sediment, silty/sandy sediment, and KeJ lava/scoria/hydrothermal breccia. The solid lines show the principal trends defined by the magmatic samples of KeJ.

Figure 11. Trace element concentrations of silty/clayey sediments (bulk and clay-size fractions) relative to the average composition of silty/sandy volcanic sediment.

Figure 12. Pyrite overgrowths on hydrothermal breccia RB-03-03-08. Pumice fragments are cemented by pyrite overgrowths to a host scoria (a & b). Close-up views of pyrite overgrowths showing bladed (c & d) and stalacitic (c) morphology. d) basaltic andesite host and e) plan view of the breccia exterior.

**Supplemental Captions**

Figure S-1 High-resolution photomosaic of the inner crater of Kick'em Jenny. Figure 1 shows the location of the surveyed area. The location of the most active gas discharging vents (Champagne and Shrimp) are marked by red stars. Note the pattern of fluid flow down the margins of the inner crater towards the relatively flat floor and the linear arrangement of diffuse vents in the lower right hand side of the image.

Figure S-2. ROV images of a) fractured hydrothermal crusts with abundant bacterial mats on the outer crater floor and b) field of small lumpy diffuse flow vents with flocculent yellowish bacterial (red laser points are 10 cm apart).

Figure S-3. Composition of KeJ silty/sandy sediment (42,32,28,26,24) and silty/clayey sediment (41,40,31,18) in the grain size range 500-63 μm. Counts were normalized to the total count. a) major sediment components b) crystal components c) scoria components.

Figure S-4. Electron microprobe SEM photographs and analyses of pyrite overgrowths on hydrothermal breccia sample RB-03-08.

Figure S-5. Plot of selected trace elements and major oxides of the altered exterior of KeJ lava/scoria/breccia relative to the fresh interior. Trace elements are in ppm. Major oxides (Fe, S) are in wt%. RB-03-03-08 (red, solid circles), RB-03-03-17 (blue, solid squares) and RB-03-03-82 (green, diamonds).

Figure S-6. Mass balance model for the alteration of silty/sandy volcanic sediment to silty/clayey sediment on the basis of wt% major oxides. The model composition is comprised of a portion of the silty/sandy volcanic sediment, clay minerals, and 1 wt% pyrite. Values for major oxide composition of the clay minerals are from the literature (see Table 8). RB-03-03-28 is the starting silty/sandy volcanic sediment and RB-03-03-18 is the alteration product used in the calculation for comparison with the model.

Movie S1. ROV video of fragile Fe-oxyhydroxide hydrothermal vents on the southeast wall of the inner crater of Kick'em Jenny volcano. Water depth 252 meters. Collected on 11/01/2013.

Movie S2. ROV video of white hydrothermal streams on the eastern wall of the inner crater of Kick'em Jenny volcano. Water depth ~260 meters. Collected on 11/01/2013.

Movie S3. ROV video of friable hydrothermal tubular mounds near the rim of the inner crater of Kick'em Jenny volcano. Water depth ~235 meters. Collected on 11/01/2013.

Movie S4. ROV video of gas collection at Champagne hydrothermal vent in the inner crater of Kick'em Jenny volcano. Water depth ~265 meters. Collected on 11/02/2013.

Movie S5. ROV video of gas flux measurement using an inverted plexiglass container at the Champagne hydrothermal vent in the inner crater of Kick'em Jenny volcano. Water depth ~265 meters. Collected on 11/13/2013.

Movie S6. ROV video of yellowish bacterial mat at the summit of Kick'em Jenny volcano. Water depth ~200 meters. Collected on 11/13/2013.

**Table 1.** Kick'em Jenny Samples

| Sample | Type | Latitude (N) | Longitude (W) | Water Depth (m) | Description |
|---|---|---|---|---|---|
| NA039-003 | ROV grab | 12.30068 | 61.63760 | 249 | reddish-orange friable vent sample |
| NA039-009 | ROV gas | 12.30131 | 61.63791 | 264 | gas sample from Champagne vent |
| NA039-010 | ROV gas | 12.30131 | 61.63790 | 264 | gas sample from Champagne vent |
| NA039-011 | ROV grab | 12.30127 | 61.63790 | 254 | indurated hydrothermal sediment from Champagne vent |
| NA039-012 | ROV core | 12.29998 | 61.63794 | 238 | fine grained reddish mud |
| NA039-059 | ROV grab | 12.30094 | 61.63793 | 262 | indurated hydrothermal sediment from Shrimp vent |
| NA039-091 | ROV gas | 12.30094 | 61.63790 | 263 | gas sample from Shrimp vent |
| NA054-068 | Niskin | 12.30068 | 61.63746 | 247 | ambient water sample at Fe-Oxide vent |
| NA054-069 | IV bag | 12.30127 | 61.63785 | 264 | Champagne vent fluid sample |
| NA054-071 | Niskin | 12.30127 | 61.63788 | 263 | ambient water sample at Champagne vent |
| NA054-072 | IV bag | 12.30070 | 61.63748 | 249 | Fe-Oxide vent fluid sample |
| NA054-076 | Niskin | 12.30184 | 61.63787 | 198 | water column sample |
| RB-03-03-08 WR | ROV grab | 12.30110 | 61.63800 | 249 | hydrothermally altered lava block |
| RB-03-03-08 P | ROV grab | 12.30110 | 61.63800 | 249 | exterior of hydrothermally altered lava block |
| RB-03-03-17 WR | ROV grab | 12.30159 | 61.63768 | 260 | hydrothermally altered lava block |
| RB-03-03-17 P | ROV grab | 12.30159 | 61.63768 | 260 | exterior of hydrothermally altered lava block |
| RB-03-03-18 | ROV core | 12.30154 | 61.63768 | 262 | gray clayed sediment from hydrothermal mound |
| RB-03-03-24 | Shipek grab | 12.30068 | 61.63810 | 235 | dark gray, coarse volcaniclastic sediment |
| RB-03-03-26 | Shipek grab | 12.29783 | 61.63807 | 222 | dark gray, coarse volcaniclastic sediment |
| RB-03-03-28 | Shipek grab | 12.30012 | 61.63765 | 234 | dark gray, coarse volcaniclastic sediment |
| RB-03-03-31 | Shipek grab | 12.30162 | 61.63765 | 267 | gray clayed sediment from hydrothermal mound |
| RB-03-03-32 | Shipek grab | 12.30207 | 61.63747 | 241 | dark gray, coarse volcaniclastic sediment |
| RB-03-03-40 | Shipek grab | 12.30078 | 61.63663 | 237 | gray clayed sediment from hydrothermal mound |
| RB-03-03-41 | Shipek grab | 12.30118 | 61.63673 | 234 | gray clayed sediment from hydrothermal mound |
| RB-03-03-42 | Shipek grab | 12.30185 | 61.63660 | 238 | dark gray, coarse volcaniclastic sediment |
| RB-03-03-67 | ROV core | 12.28722 | 61.62165 | 257 | carbonate sediment |
| RB-03-03-82 WR | ROV grab | 12.30133 | 61.63780 | 250 | hydrothermally altered lava block |
| RB-03-03-82 P | ROV grab | 12.30133 | 61.63780 | 250 | hydrothermally altered lava block |
| RB-03-03-85 P | ROV grab | 12.30133 | 61.63791 | 256 | hydrothermally altered lava block |

**Table 2.** Fluid densities of Kick'em Jenny crater samples

| Sample | Type | Depth (m) | Density g/cm3 | No. Analyses | Std. Dev. | Salinity[1] | Description |
|---|---|---|---|---|---|---|---|
| NA054-068 | Niskin | 247 | 1.025385 | 3 | 0.000007 | 35.815 | Ambient water sample at Fe-Oxide vent |
| NA054-069 | IV bag | 264 | 1.025594 | 4 | 0.000001 | 36.089 | Champagne vent fluid sample |
| NA054-071 | Niskin | 263 | 1.025355 | 4 | 0.000011 | 35.776 | Ambient water sample at Champagne vent |
| NA054-072 | IV bag | 249 | 1.025263 | 4 | 0.000002 | 35.655 | Fe-Oxide vent fluid sample |
| NA054-076 | Niskin | 198 | 1.025697 | 4 | 0.000006 | 36.224 | Water column sample |

1. Salinity calculated from fluid density at 20$^{o}$ C using Fofonoff, P. and R. C. Millard Jr (1983) Algorithms for computation of fundamental properties of seawater.Unesco Technical Papers in Marine Sciences 44, 53 pp.

**Table 3.** Analyses of Gas Samples from Kick'em Jenny Crater

| Gas | NA039-009 Champagne Vent Top | NA039-010 Champagne Vent Side | NA039-091 Shrimp Vent | Arc Average[1] | units |
|---|---|---|---|---|---|
| $TCO_2$ | 92.77 | 92.80 | 96.38 | 97.24 | % |
| $N_2$ | 1.83 | 2.38 | 1.78 | 1.97 | % |
| $CH_4$ | 0.21 | 0.29 | 0.05 | 0.02 | % |
| $H_2$ | 0.47 | 0.51 | 0.56 | 0.01 | % |
| $O_2$ | 0.02 | 0.02 | 0.13 | | % |
| Ne | 0.015 | 0.016 | 0.019 | | % |
| Ar | 0.003 | 0.010 | 0.011 | 0.03 | % |
| CO | 0.00 | 0.00 | 0.00 | | % |
| $N_2O$ | 0.00 | 0.00 | 0.00 | | % |
| $C_2H_2$ | 0.05 | 0.00 | 0.02 | | ppm |
| $C_2H_4$ | 0.00 | 0.00 | 0.00 | | ppm |
| $C_2H_6$ | 0.00 | 45.72 | 6.14 | | ppm |
| $C_3H_4$ | 0.18 | 0.05 | 0.03 | | ppm |
| $C_3H_6$+$H_8$ | 2.82 | 2.82 | 0.29 | | ppm |
| $nC_4H_{10}$ | 0.90 | 1.19 | 0.12 | | ppm |
| $iC_4H_{10}$ | 0.23 | 0.30 | 0.00 | | ppm |
| Helium | 13.50 | 17.50 | 6.87 | 21.5 | ppmv |
| Neon | 0.02 | 0.03 | 0.252 | 0.375 | ppmv |
| He/Ne | 610 | 525 | 27 | 57 | |
| $^3He/^4He$ | 6.68 | 6.69 | 6.82 | 6.79 | $R/R_{air}$ |
| Depth (m) | 264 | 264 | 263 | | |

1. Average of gases collected at NW Rota, Daikoku, Nikko, Giggenbach and Volcano-1 submarine volcanoes from Lupton et al., 2008.

**Table 4.** Gas Flux Measurements at Champagne Vent Mound

1. Champagne Summit Vent

| *Measurement* | *Time (s)* | *Vol. (cc)* | *Temp.* | *Flux (cc/s)* | *Depth (m)* | *P (Atms)* | *Moles/cc* | *Moles/s* | $CO_2$ g/s | $CO_2$ kg/day |
|---|---|---|---|---|---|---|---|---|---|---|
| 1 | 70 | 2000 | 107 | 28.6 | 264 | 27.2 | 0.0009 | 0.0229 | 1.0 | 87 |
| 2 | 62 | 2000 | 107 | 32.3 | 264 | 27.2 | 0.0009 | 0.0259 | 1.1 | 98 |
| 3 | 55 | 2000 | 107 | 36.4 | 264 | 27.2 | 0.0009 | 0.0292 | 1.3 | 111 |
| 4 | 57 | 2000 | 107 | 35.1 | 264 | 27.2 | 0.0009 | 0.0282 | 1.2 | 107 |
| *Average* | | | | 33.1 | | | | | 1.2 | 101 |
| *Std. Dev.* | | | | 3.0 | | | | | 0.1 | 9 |

2. Champagne Side Vent

| *Measurement* | *Time (s)* | *Vol. (cc)* | *Temp.* | *Flux (cc/s)* | *Depth (m)* | *P (Atms)* | *Moles/cc* | *Moles/s* | $CO_2$ g/s | $CO_2$ kg/day |
|---|---|---|---|---|---|---|---|---|---|---|
| 1 | 1295 | 2000 | 16 | 1.5 | 263 | 27.1 | 0.0011 | 0.0016 | 0.1 | 6 |

3. Shrimp Vent

| Measurement | Time (s) | Vol. (cc) | Temp. | Flux (cc/s) | Depth (m) | P (Atms) | Moles/cc | Moles/s | $CO_2$ g/s | $CO_2$ kg/day |
|---|---|---|---|---|---|---|---|---|---|---|
| 1 | 244 | 2000 | 28 | 8.2 | 262 | 27.0 | 0.0011 | 0.0085 | 0.4 | 32 |
| 2 | 218 | 2000 | 28 | 9.2 | 262 | 27.0 | 0.0011 | 0.0095 | 0.4 | 36 |
| 3 | 206 | 2000 | 28 | 9.7 | 262 | 27.0 | 0.0011 | 0.0101 | 0.4 | 38 |
| *Average* | | | | 9.0 | | | | | 0.4 | 36 |
| *Std. Dev.* | | | | 0.6 | | | | | 0.0 | 2 |

**Table 5.** X-Ray Diffraction Models for Kick'em Jenny Hydrothermal Deposits[1]

| Phase | RB-03-03-18 | RB-03-03-40 | NA039-03 | NA039-11 | NA039-12 | NA039-59 |
|---|---|---|---|---|---|---|
| Plagioclase (An40) | 49.7 | 53.1 | 2.0 | 60.7 | 2.1 | 15.3 |
| Labradorite (An66) | | | | | | |
| Smectite (di-oct) | 16.3 | 12.3 | | | | |
| Talc | 12.1 | 11.6 | | 4.3 | | 2.5 |
| Illite (di-oct) | 6.8 | 10.5 | | | | |
| I/S mixed layer clay (di-oct) | 5.3 | 3.8 | | | | |
| Amorphous silica | | | 48.5 | | 23.5 | 58.0 |
| Ferrihydrite (cubic) | | | 39.5 | | 59.0 | 5.6 |
| Goethite | | | 8.3 | | 15.1 | |
| Barite | | | | 0.6 | | 3.0 |
| Nontronite | | | 1.3 | 24.4 | | 5.6 |
| Cristobalite | | | 0.2 | | | |
| Diopside | 4.4 | 3 | | 2.6 | | |
| Vermiculite | 1.7 | 1.9 | | | | |
| Actinolite | 1.6 | 1.1 | | 3.2 | | 1.0 |
| Clinochlore | | | | | | 1.3 |
| Tremolite | | | | | | 4.9 |
| Pyrite | 1.3 | 0.9 | | 3.1 | | 2.3 |
| Quartz | 0.8 | 0.9 | | 1.1 | 0.2 | |
| Magnesite | | 0.9 | | | | |
| Magnetite | | | | | 0.1 | |
| Bassanite (trigonal) | | | | | | 0.4 |

1. XRD models produced using RIQAS for whole-pattern fitting of x-ray or neutron powder diffraction data

**Table 6.** Major Element Composition of Kick'em Jenny Crater Samples

| Sample | $SiO_2$ | $TiO_2$ | $Al_2O_3$ | $Fe_2O_3$* | MnO | MgO | CaO | $Na_2O$ | $K_2O$ | $P_2O_5$ | S | Total | LOI |
|---|---|---|---|---|---|---|---|---|---|---|---|---|---|
| NA039-003 | 48.53 | 0.09 | 1.40 | 40.95 | 0.03 | 1.31 | 1.42 | 3.18 | 0.28 | 1.44 | 0.49 | 99.12 | 17.38 |
| NA039-011 | 50.26 | 0.91 | 19.80 | 8.94 | 0.08 | 5.94 | 8.67 | 3.31 | 0.41 | 0.11 | 3.36 | 101.79 | 7.72 |
| NA039-012 | 27.20 | 0.15 | 2.50 | 59.02 | 0.04 | 1.75 | 1.89 | 2.12 | 0.34 | 1.51 | 0.20 | 96.72 | 20.57 |
| NA039-059 | 55.17 | 0.71 | 13.77 | 11.58 | 0.05 | 4.84 | 3.14 | 1.94 | 0.44 | 0.07 | 7.38 | 99.09 | 14.70 |
| RB-03-03-08 WR | 54.84 | 0.71 | 19.52 | 8.38 | 0.19 | 3.27 | 8.01 | 3.65 | 1.18 | 0.17 | 0.01 | 99.92 | 0.50 |
| RB-03-03-08 P | 34.11 | 0.58 | 12.95 | 38.37 | 0.08 | 3.31 | 6.26 | 2.53 | 0.52 | 0.08 | 8.84 | 98.79 | 14.65 |
| RB-03-03-17 WR | 55.15 | 0.71 | 19.44 | 7.50 | 0.17 | 3.79 | 8.35 | 3.35 | 1.15 | 0.17 | 0.21 | 99.78 | 1.00 |
| RB-03-03-17 P | 55.79 | 0.73 | 19.46 | 6.97 | 0.16 | 3.68 | 8.35 | 3.53 | 1.20 | 0.17 | 1.10 | 100.04 | 2.02 |
| RB-03-03-18 | 52.84 | 0.93 | 16.73 | 10.31 | 0.16 | 7.84 | 6.94 | 3.28 | 0.71 | 0.15 | 1.38 | 99.89 | 6.50 |
| RB-03-03-24 | 50.49 | 0.94 | 20.34 | 7.99 | 0.15 | 5.57 | 10.84 | 2.75 | 0.68 | 0.12 | 0.18 | 99.87 | 1.23 |
| RB-03-03-26 | 50.78 | 0.86 | 20.43 | 8.24 | 0.16 | 5.07 | 10.40 | 3.10 | 0.75 | 0.11 | 0.23 | 99.90 | 1.12 |
| RB-03-03-28 | 50.61 | 0.98 | 20.40 | 8.32 | 0.14 | 5.17 | 10.81 | 2.94 | 0.63 | 0.10 | 0.52 | 100.10 | 1.39 |
| RB-03-03-31 | 52.04 | 0.97 | 18.35 | 9.59 | 0.15 | 6.13 | 8.16 | 3.40 | 0.68 | 0.15 | 1.49 | 99.62 | 4.05 |
| RB-03-03-32 | 52.17 | 0.83 | 19.78 | 8.28 | 0.14 | 4.57 | 10.27 | 2.82 | 0.67 | 0.14 | 0.21 | 99.67 | 2.19 |
| RB-03-03-40 | 57.19 | 0.84 | 16.05 | 8.44 | 0.13 | 5.73 | 7.03 | 3.28 | 0.67 | 0.16 | 0.92 | 99.52 | 5.39 |
| RB-03-03-41 | 61.05 | 0.75 | 15.07 | 7.57 | 0.12 | 4.53 | 6.88 | 2.93 | 0.65 | 0.16 | 0.70 | 99.71 | 4.08 |
| RB-03-03-42 | 49.10 | 1.01 | 19.30 | 8.92 | 0.15 | 6.94 | 11.41 | 2.64 | 0.62 | 0.12 | 0.20 | 100.21 | 1.31 |
| RB-03-03-67 | 26.03 | 0.34 | 7.94 | 3.76 | 0.10 | 5.35 | 53.14 | 0.58 | 0.12 | 0.21 | 0.22 | 97.57 | 33.56 |
| RB-03-03-82 WR | 47.92 | 1.15 | 18.37 | 8.91 | 0.16 | 8.09 | 11.60 | 2.64 | 0.69 | 0.08 | 0.00 | 99.61 | -0.03 |
| RB-03-03-82 P | 48.19 | 1.11 | 18.81 | 8.89 | 0.15 | 7.35 | 11.65 | 2.57 | 0.70 | 0.09 | 0.40 | 99.51 | 0.25 |
| RB-03-03-85 P | 55.50 | 0.84 | 16.26 | 9.96 | 0.12 | 4.98 | 9.22 | 2.29 | 0.54 | 0.05 | 4.13 | 99.76 | 5.15 |

Units are wt% and $Fe_2O_3$* is total Fe. LOI is loss on ignition.

**Table 7.** Trace Element Composition of Kick'em Jenny Crater Samples

| Sample | Li | Be | Sc | TiO2 | V | Cr | Co | Ni | Cu | Zn | Ga | As | Rb | Sr | Y | Zr | Nb | Cs | Ba | La | Ce | Hf | Ta | Pb | Th | U | Sb | Tl | Bi |
|---|---|---|---|---|---|---|---|---|---|---|---|---|---|---|---|---|---|---|---|---|---|---|---|---|---|---|---|---|---|
| NA039-003 | | | | 0.02 | 50 | 17 | | 0 | | 10 | 2 | | 8.9 | 151 | 0.7 | 9 | 0.1 | | 48 | 0 | 0 | | | 3 | 0 | 2 | | | |
| NA039-011 | | | | 0.92 | 233 | 83 | | 38 | | 68 | 16 | | 16.2 | 619 | 18.2 | 81 | 3.8 | | 4605 | 6 | 21 | | | 2 | 0 | 0 | | | |
| NA039-012 | | | | 0.11 | 132 | 27 | | 0 | | 21 | 2 | | 7.3 | 306 | 2.0 | 12 | 0.6 | | 122 | 0 | 1 | | | 8 | 0 | 0 | | | |
| NA039-059 | | | | 0.81 | 240 | 47 | | 31 | | 261 | 8 | | 18.2 | 1619 | 11.1 | 65 | 2.5 | | 46000 | 0 | 0 | | | 0 | 0 | 2 | | | |
| RB-03-03-08 WR | 11.6 | 1.4 | 14.5 | 0.68 | 143.7 | 6.7 | 19.1 | 8.5 | 108.6 | 90.9 | 19.9 | 7.76 | 50.5 | 334.4 | 23.3 | 117.3 | 6.95 | 1.61 | 245.6 | 11.31 | 22.5 | 2.82 | 0.40 | 6.12 | 4.30 | 2.24 | 0.20 | 0.38 | 0.25 |
| RB-03-03-08 P | 3.5 | 0.6 | 19.1 | 0.48 | 133.2 | 101.7 | 13.8 | 24.4 | 44.0 | 22.6 | 12.4 | 1.45 | 13.3 | 199.6 | 10.0 | 31.0 | 3.46 | 0.43 | 92.3 | 4.98 | 9.7 | 0.99 | 0.22 | 4.09 | 1.65 | 0.72 | 0.06 | 0.23 | 0.03 |
| RB-03-03-17 WR | 2.2 | 1.4 | 17.6 | 0.65 | 130.4 | 38.9 | 17.7 | 21.0 | 49.7 | 87.0 | 19.0 | 3.35 | 38.8 | 369.3 | 16.7 | 95.5 | 9.85 | 0.31 | 237.8 | 12.73 | 23.4 | 2.17 | 0.65 | 4.70 | 3.96 | 1.96 | 0.13 | 0.37 | 0.01 |
| RB-03-03-17 P | 2.4 | 1.4 | 18.4 | 0.69 | 138.3 | 38.5 | 17.5 | 21.2 | 51.7 | 72.5 | 20.1 | 3.55 | 40.9 | 385.5 | 17.3 | 98.9 | 10.20 | 0.31 | 254.1 | 13.09 | 24.1 | 2.20 | 0.63 | 4.90 | 4.10 | 1.98 | 0.09 | 0.63 | 0.01 |
| RB-03-03-18 | 6.5 | 1.0 | 31.2 | 0.86 | 235.6 | 79.5 | 24.0 | 47.1 | 134.4 | 47.0 | 19.3 | 12.02 | 23.7 | 264.2 | 19.9 | 70.6 | 5.52 | 0.95 | 171.7 | 8.48 | 18.0 | 1.92 | 0.30 | 7.34 | 2.56 | 1.47 | 0.23 | 0.77 | 0.27 |
| RB-03-03-24 | 7.8 | 0.9 | 36.0 | 0.86 | 243.1 | 132.7 | 21.1 | 38.1 | 57.6 | 114.5 | 18.4 | 4.72 | 24.0 | 323.9 | 20.0 | 62.6 | 4.04 | 0.77 | 133.2 | 5.86 | 12.3 | 1.76 | 0.24 | 3.45 | 1.90 | 1.18 | 0.10 | 0.23 | 0.06 |
| RB-03-03-26 | 10.6 | 1.0 | 31.8 | 0.87 | 220.4 | 98.3 | 23.6 | 36.1 | 70.4 | 157.2 | 20.8 | 3.88 | 24.4 | 330.4 | 17.5 | 60.2 | 4.65 | 1.02 | 135.1 | 5.59 | 12.9 | 1.70 | 0.30 | 3.40 | 1.73 | 0.94 | 0.09 | 0.31 | 0.09 |
| RB-03-03-28 | 8.5 | 0.9 | 36.6 | 1.01 | 254.0 | 117.7 | 24.2 | 46.5 | 75.0 | 73.1 | 18.0 | 3.88 | 24.4 | 330.4 | 17.5 | 60.2 | 4.65 | 1.02 | 135.1 | 5.59 | 12.9 | 1.70 | 0.30 | 3.40 | 1.73 | 0.94 | 0.09 | 0.31 | 0.09 |
| RB-03-03-31 | 7.4 | 1.0 | 31.1 | 0.97 | 240.9 | 86.4 | 33.8 | 57.4 | 181.3 | 104.0 | 20.9 | 10.37 | 26.9 | 288.7 | 21.7 | 68.6 | 5.78 | 1.81 | 172.9 | 8.68 | 19.4 | 1.93 | 0.36 | 6.41 | 2.36 | 1.70 | 0.22 | 2.33 | 0.21 |
| RB-03-03-32 | 7.5 | 0.9 | 31.5 | 0.83 | 224.1 | 99.1 | 20.9 | 35.8 | 59.8 | 81.3 | 18.4 | 4.16 | 26.0 | 339.6 | 17.7 | 66.2 | 4.33 | 0.91 | 143.8 | 5.84 | 12.9 | 1.82 | 0.28 | 8.23 | 1.97 | 1.21 | 0.14 | 2.13 | 0.06 |
| RB-03-03-40 | 7.0 | 0.9 | 25.6 | 0.74 | 196.3 | 68.2 | 20.4 | 38.1 | 91.5 | 58.7 | 16.5 | 19.03 | 27.4 | 253.8 | 17.2 | 60.2 | 4.88 | 2.61 | 164.0 | 7.26 | 15.1 | 1.60 | 0.30 | 6.50 | 2.30 | 1.21 | 0.20 | 1.13 | 0.18 |
| RB-03-03-41 | 6.6 | 0.8 | 22.1 | 0.65 | 169.9 | 64.4 | 17.2 | 30.2 | 80.6 | 39.2 | 14.3 | 14.25 | 22.2 | 239.9 | 14.9 | 46.3 | 4.13 | 1.25 | 142.3 | 6.07 | 12.8 | 1.40 | 0.24 | 5.55 | 1.92 | 1.01 | 0.15 | 0.73 | 0.13 |
| RB-03-03-42 | 7.5 | 0.7 | 46.5 | 0.99 | 269.6 | 177.2 | 28.3 | 61.0 | 64.9 | 35.6 | 16.9 | 4.97 | 21.1 | 304.1 | 18.8 | 61.7 | 3.99 | 0.65 | 120.2 | 4.96 | 11.7 | 1.74 | 0.25 | 3.62 | 1.63 | 0.93 | 0.09 | 0.27 | 0.06 |
| RB-03-03-67 | 13.3 | 0.6 | 7.6 | 0.23 | 54.6 | 61.8 | 7.3 | 37.9 | 23.7 | 34.9 | 5.3 | 5.09 | 12.5 | 2900.8 | 8.6 | 19.7 | 2.71 | 0.85 | 77.9 | 7.51 | 12.9 | 0.63 | 0.16 | 8.59 | 2.37 | 2.50 | 0.32 | 0.12 | 0.06 |
| RB-03-03-82 WR | 8.8 | 0.7 | 59.0 | 1.13 | 327.6 | 194.6 | 34.1 | 70.3 | 69.6 | 55.7 | 16.8 | 3.59 | 22.9 | 300.1 | 21.7 | 67.4 | 4.39 | 0.69 | 127.6 | 5.53 | 12.5 | 1.86 | 0.26 | 3.09 | 1.75 | 0.92 | 0.10 | 0.09 | 0.02 |
| RB-03-03-82 P | 8.6 | 0.7 | 55.8 | 1.09 | 315.4 | 181.9 | 31.9 | 65.2 | 75.6 | 54.2 | 17.0 | 3.98 | 23.2 | 304.4 | 21.0 | 68.0 | 4.37 | 0.70 | 127.2 | 5.58 | 12.5 | 1.83 | 0.26 | 3.13 | 1.76 | 0.94 | 0.09 | 0.08 | 0.02 |

Units are in ppm except for $TiO_2$ in wt.%. NA039 samples determined by XRF and RB-03-03 samples determined by ICPMS

**Appendix Table 8.** Mixing model to assess hydrothermal alternation of primary volcanic sediment at Kick'em Jenny

| **Sample Data**[1] | $SiO_2$ wt % | MgO wt % | $Al_2O_3$ wt % | $Na_2O$ wt % | $K_2O$ wt % | CaO wt % | $TiO_2$ wt % | $Fe_2O_3$* wt % |
|---|---|---|---|---|---|---|---|---|
| **RB-03-03-28** | 50.68 | 5.18 | 20.43 | 2.94 | 0.63 | 10.83 | 0.98 | 8.33 |
| talc | 61.92 | 21.79 | 0.69 | 0.34 | 0.01 | 0.02 | 0.01 | 15.21 |
| smectite | 53.22 | 15.94 | 3.85 | 3.65 | 0.24 | 0.00 | 1.32 | 21.77 |
| smectite | 40.62 | 1.78 | 3.97 | 1.09 | 0.14 | 0.00 | 6.79 | 45.63 |
| illite | 58.42 | 1.04 | 34.95 | 1.33 | 3.87 | 0.00 | 0.10 | 0.29 |
| illite | 57.26 | 0.99 | 35.26 | 1.36 | 4.21 | 0.08 | 0.58 | 0.27 |
| **RB-03-03-18** | 52.68 | 7.39 | 17.36 | 3.13 | 0.73 | 7.46 | 0.93 | 10.32 |
| | | | | | | | | |
| **Model Calculation**[2] | | | | | | | | |
| talc 17% | 10.53 | 3.70 | 0.12 | 0.06 | 0.00 | 0.00 | 0.00 | 2.59 |
| smectite 3% | 1.22 | 0.05 | 0.12 | 0.03 | 0.00 | 0.00 | 0.20 | 1.37 |
| illite 4% | 2.34 | 0.04 | 1.40 | 0.05 | 0.15 | 0.00 | 0.00 | 0.01 |
| illite/smectite 4% | 2.24 | 0.22 | 1.03 | 0.08 | 0.12 | 0.00 | 0.03 | 0.27 |
| RB-03-03-28 71% | 35.98 | 3.68 | 14.50 | 2.09 | 0.45 | 7.69 | 0.70 | 5.92 |
| pyrite 1% | | | | | | | | 0.4655 |
| **Total** | **52.31** | **7.69** | **17.17** | **2.32** | **0.73** | **7.69** | **0.94** | **10.62** |
| 100 | | | | | | | | |
| | | | | | | | | |
| **Model Comparison**[3] | | | | | | | | |
| RB-03-03-28 | 50.68 | 5.18 | 20.43 | 2.94 | 0.63 | 10.83 | 0.98 | 8.33 |
| Best fit result | 52.31 | 7.69 | 17.17 | 2.32 | 0.73 | 7.69 | 0.94 | 10.62 |
| % difference | 3 | 49 | -16 | -21 | 16 | -29 | -4 | 27 |
| | | | | | | | | |
| **Sample Comparison**[4] | | | | | | | | |
| RB-03-03-28 | 50.68 | 5.18 | 20.43 | 2.94 | 0.63 | 10.83 | 0.98 | 8.33 |
| RB-03-03-18 | 52.68 | 7.39 | 17.36 | 3.13 | 0.73 | 7.46 | 0.93 | 10.32 |
| % difference | 4 | 43 | -15 | 6 | 16 | -31 | -5 | 24 |

1. Analyses of talc, smectite and illite from Cole, 1988; Turner et al., 1993; Severmann et al., 2004; Lackschewitz et al., 2004; Dekov et al., 2008a,b and Cuadros et al., 2008
2. Model calculations based on least squares fit of RB-03-03-28 plus talc, smectite, and illite to yield hydrothermal mound sediment RB-03-03-18
3. Model comparison shows the percentage change of each element from the starting primary sediment (RB-03-03-28) to the best fit model of hydrothermal mound sediment
4. Sample comparison showe the percentage change of each element between the primary sediment (RB-03-03-28) and the hydrothermal mound sediment (RB-03-03-18)

**Figure 1 (next page)**

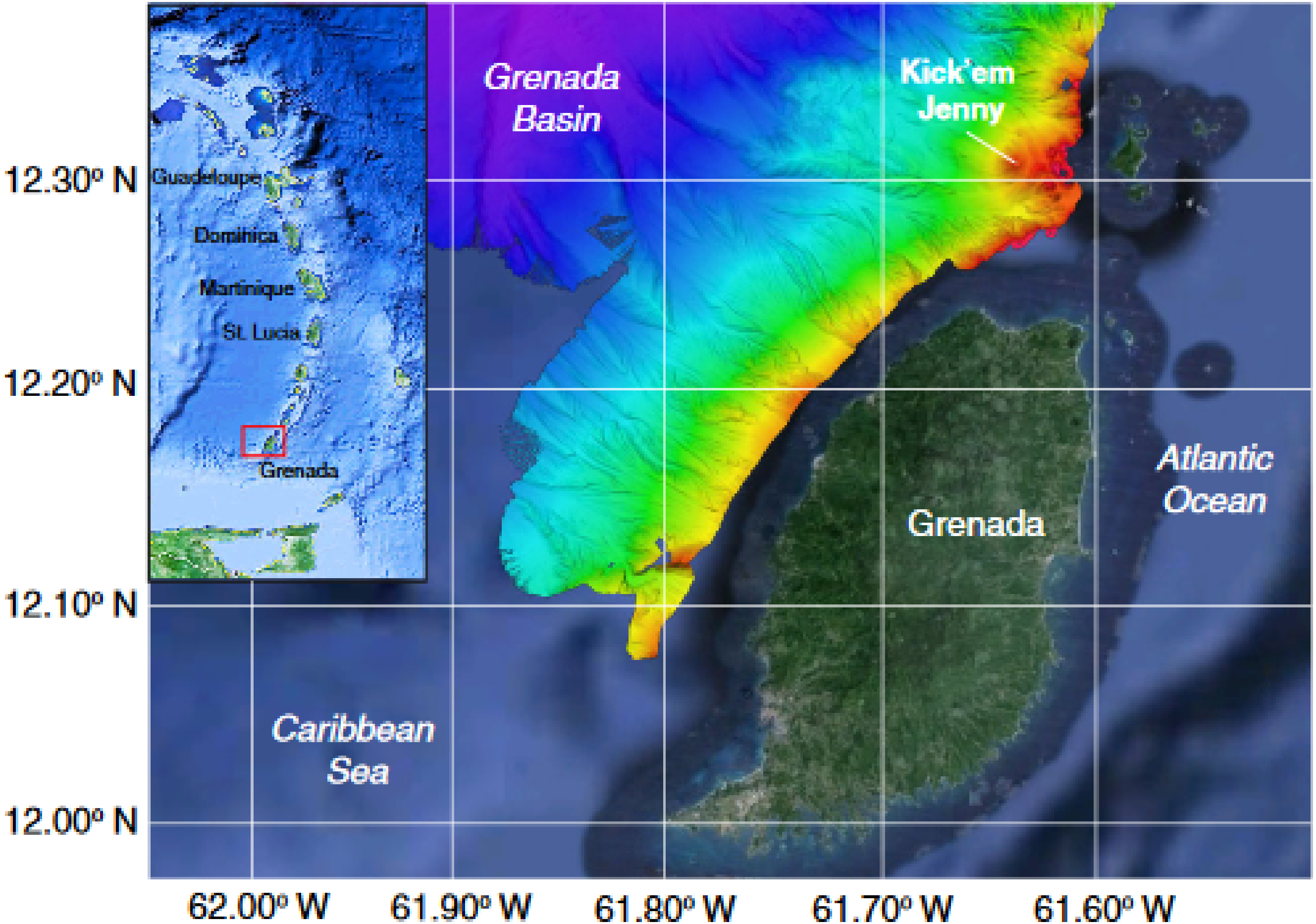

Grenada
Basin
Kick'em
Jenny
Guadeloupe
Dominica
Martinique
St. Lucia
Grenada
Atlantic
Ocean
Grenada
Caribbean
Sea
12.30° N
12.20° N
12.10° N
12.00° N
62.00° W
61.90° W
61.80° W
61.70° W
61.60° W

**Figure 2 (next page)**

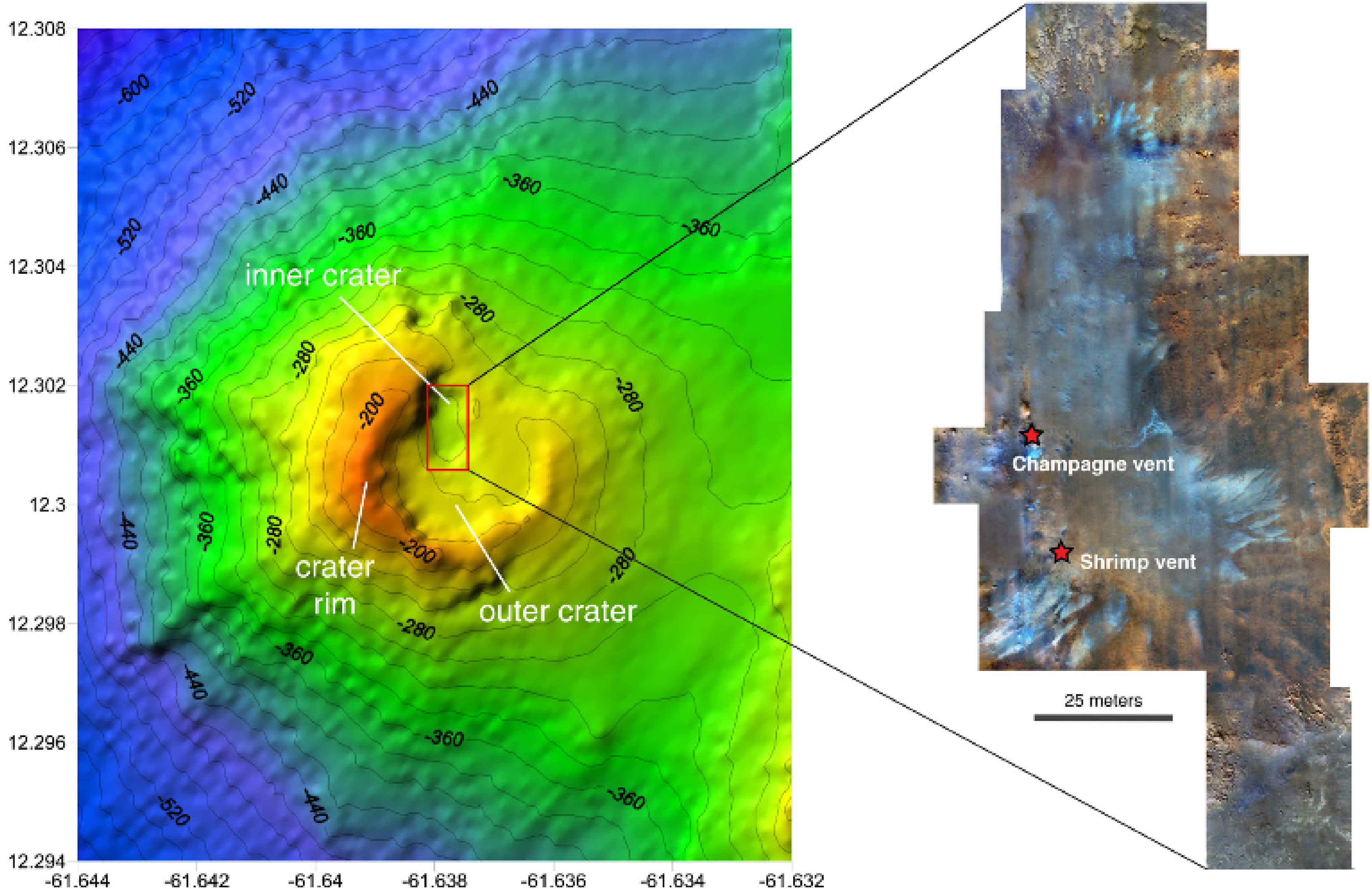

inner crater
crater rim
outer crater
Champagne vent
Shrimp vent
25 meters
-600
-520
-440
-360
-280
-200
12.308
12.306
12.304
12.302
12.3
12.298
12.296
12.294
-61.644
-61.642
-61.64
-61.638
-61.636
-61.634
-61.632

**Figure 3 (next page)**

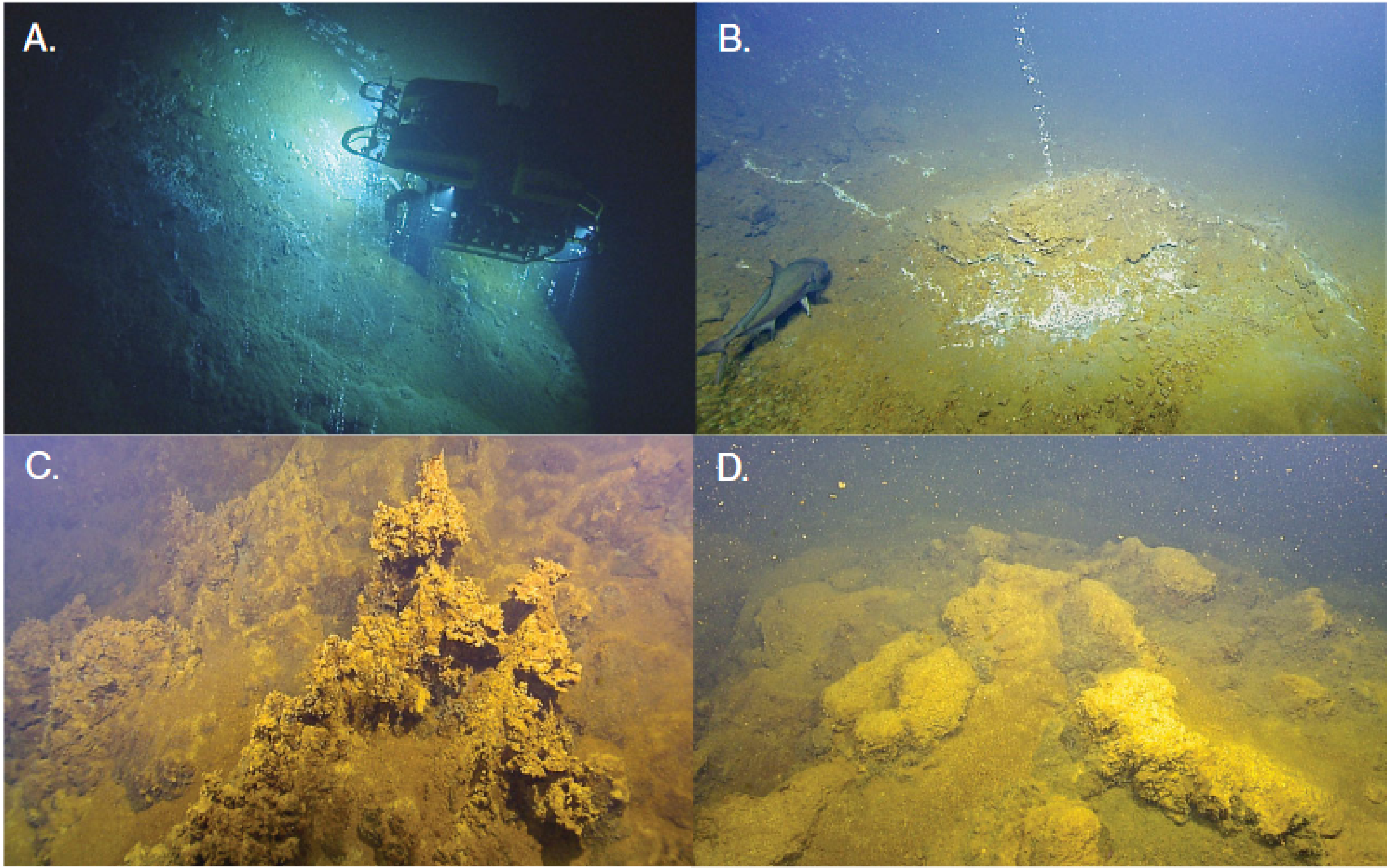
A.
B.
C.
D.

**Figure 4 (next page)**

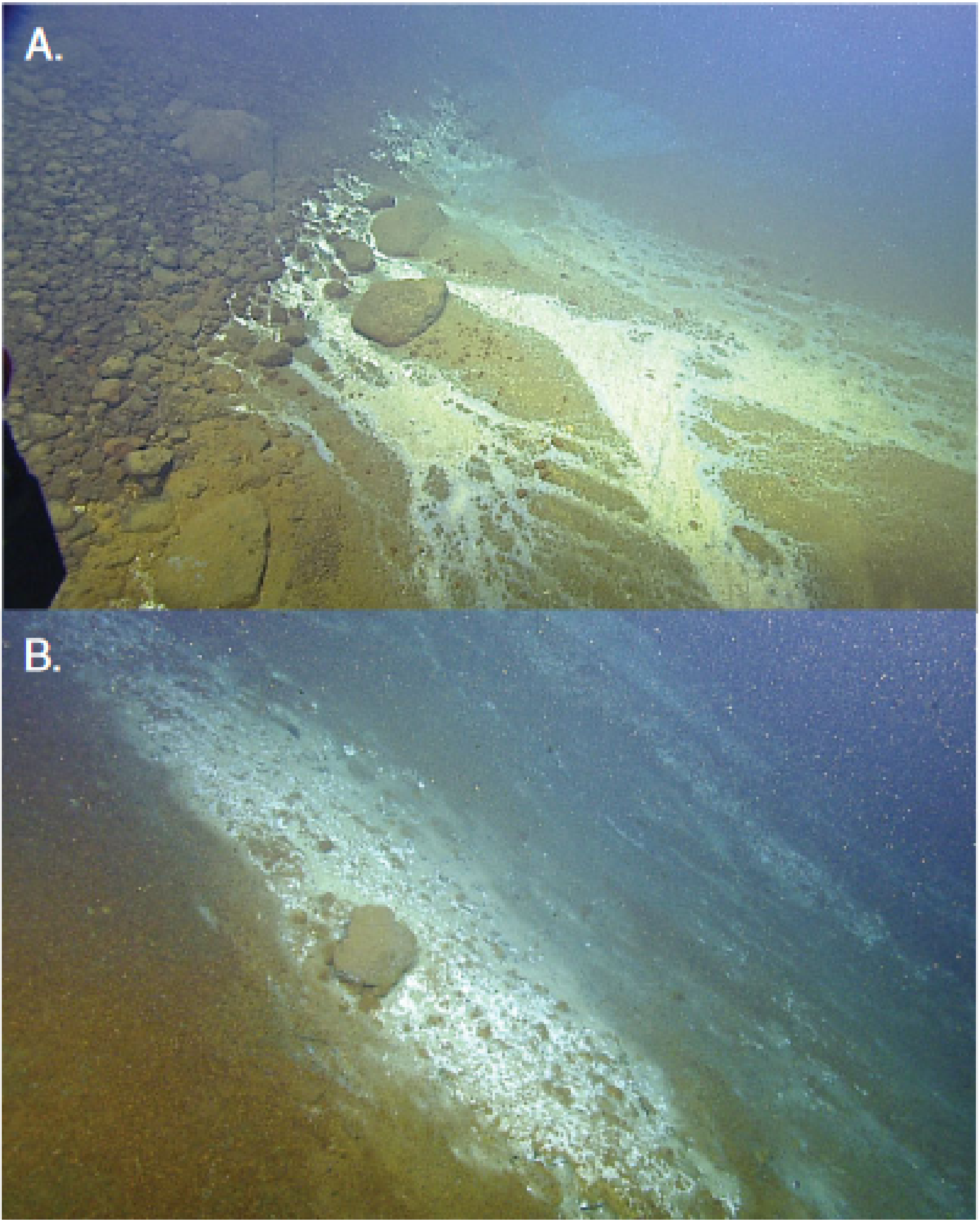
A.
B.

**Figure 5 (next page)**

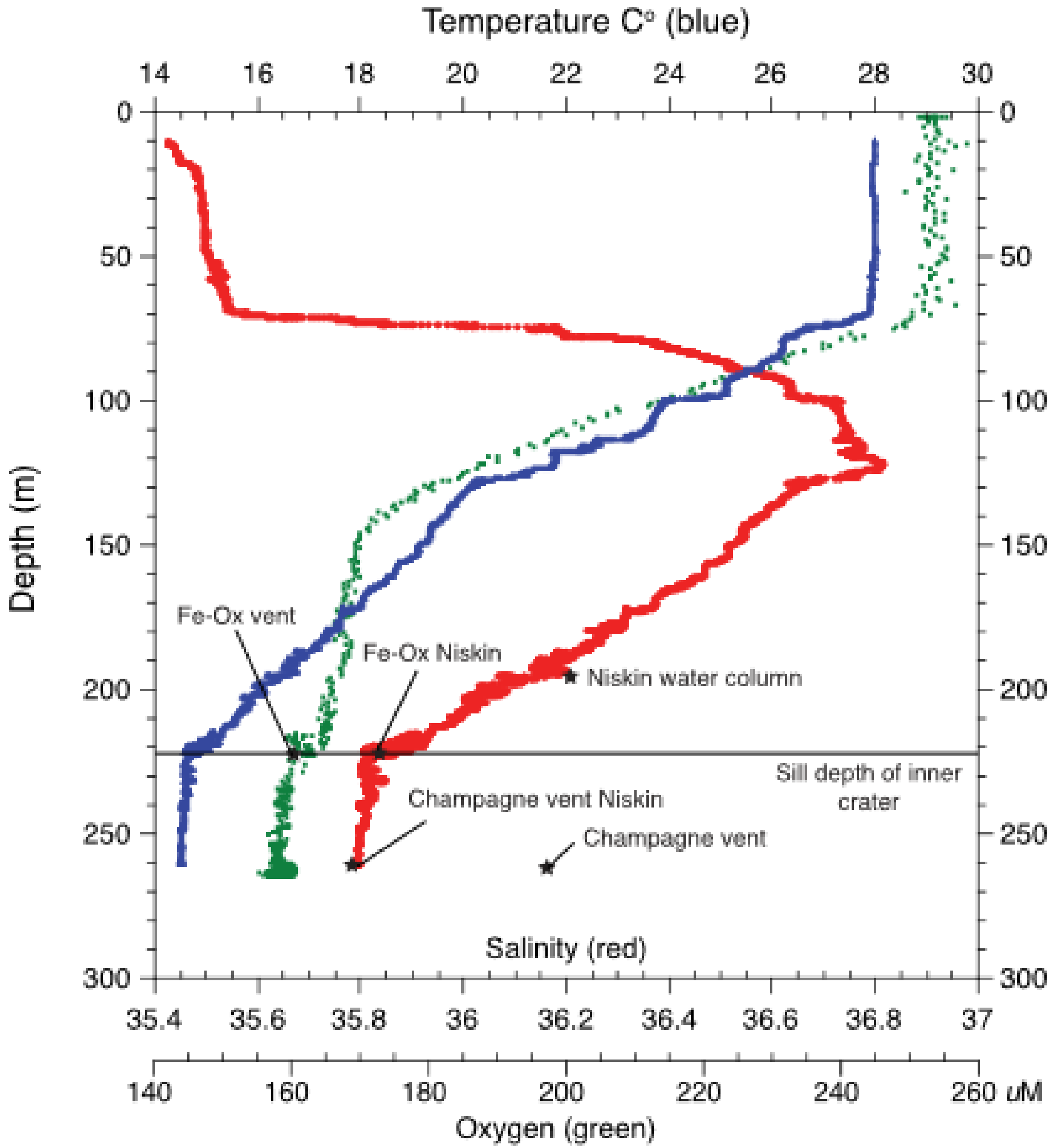

Temperature C° (blue)
14
16
18
20
22
24
26
28
30
Depth (m)
0
50
100
150
200
250
300
Fe-Ox vent
Fe-Ox Niskin
Niskin water column
Sill depth of inner crater
Champagne vent Niskin
Champagne vent
Salinity (red)
35.4
35.6
35.8
36
36.2
36.4
36.6
36.8
37
140
160
180
200
220
240
260 uM
Oxygen (green)

**Figure 6 (next page)**

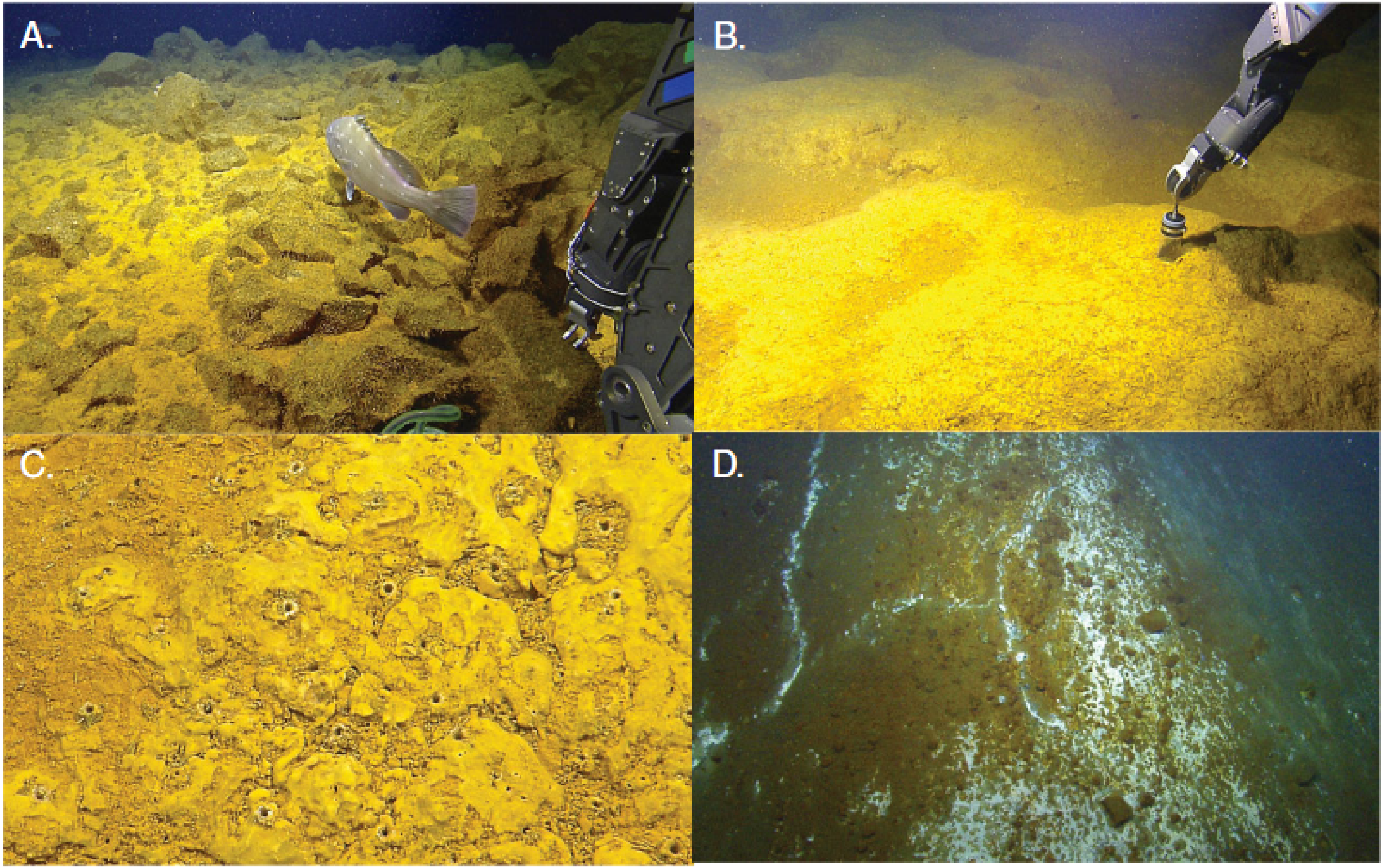
A.
B.
C.
D.

**Figure 7 (next page)**

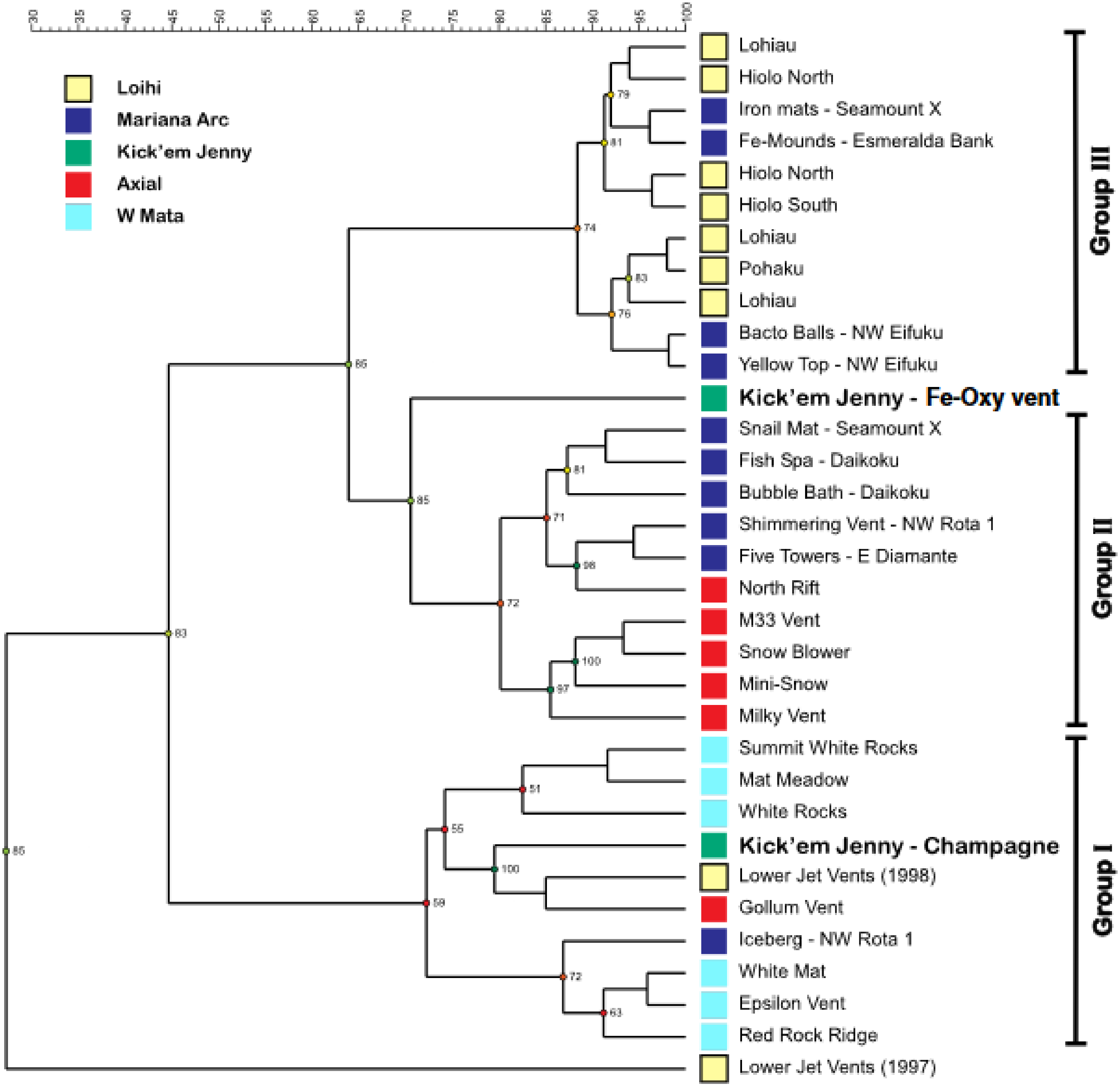

Loihi
Mariana Arc
Kick'em Jenny
Axial
W Mata
Lohiau
Hiolo North
Iron mats - Seamount X
Fe-Mounds - Esmeralda Bank
Hiolo North
Hiolo South
Lohiau
Pohaku
Lohiau
Bacto Balls - NW Eifuku
Yellow Top - NW Eifuku
Kick'em Jenny - Fe-Oxy vent
Snail Mat - Seamount X
Fish Spa - Daikoku
Bubble Bath - Daikoku
Shimmering Vent - NW Rota 1
Five Towers - E Diamante
North Rift
M33 Vent
Snow Blower
Mini-Snow
Milky Vent
Summit White Rocks
Mat Meadow
White Rocks
Kick'em Jenny - Champagne
Lower Jet Vents (1998)
Gollum Vent
Iceberg - NW Rota 1
White Mat
Epsilon Vent
Red Rock Ridge
Lower Jet Vents (1997)
Group III
Group II
Group I

**Figure 8 (next page)**

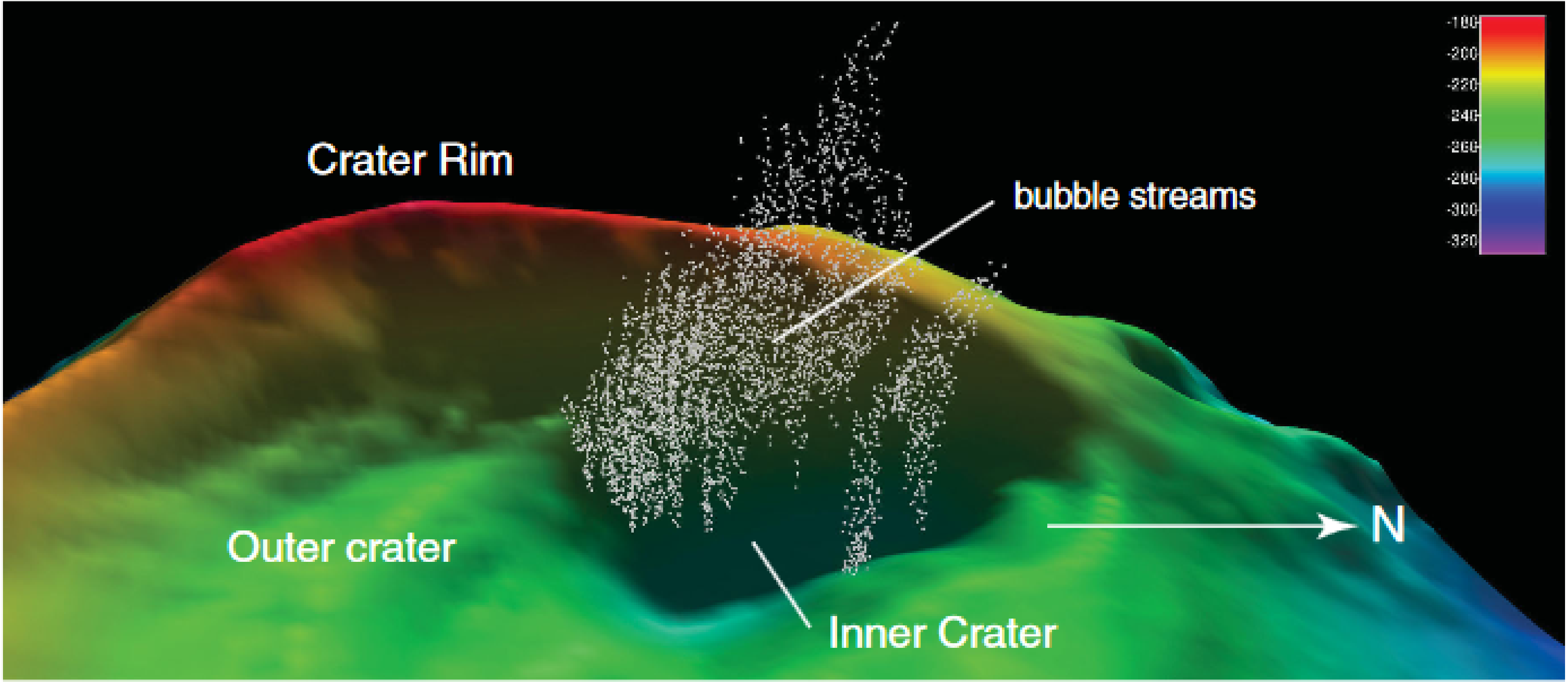

Crater Rim
bubble streams
Outer crater
Inner Crater
N

**Figure 9 (next page)**

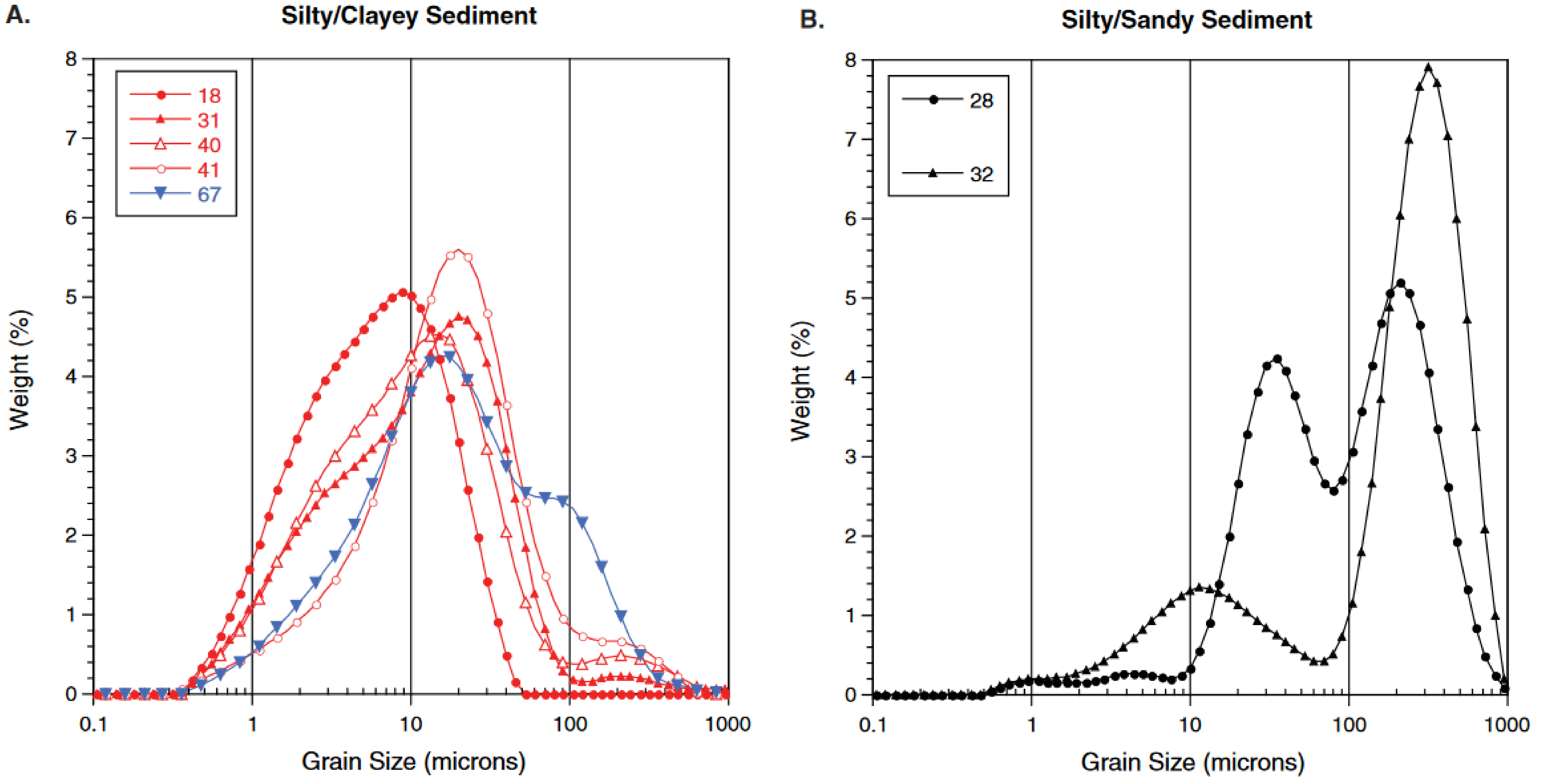

A.
Silty/Clayey Sediment
18
31
40
41
67
Weight (%)
Grain Size (microns)
0.1
1
10
100
1000
0
1
2
3
4
5
6
7
8
B.
Silty/Sandy Sediment
28
32
Weight (%)
Grain Size (microns)

**Figure 10 (next page)**

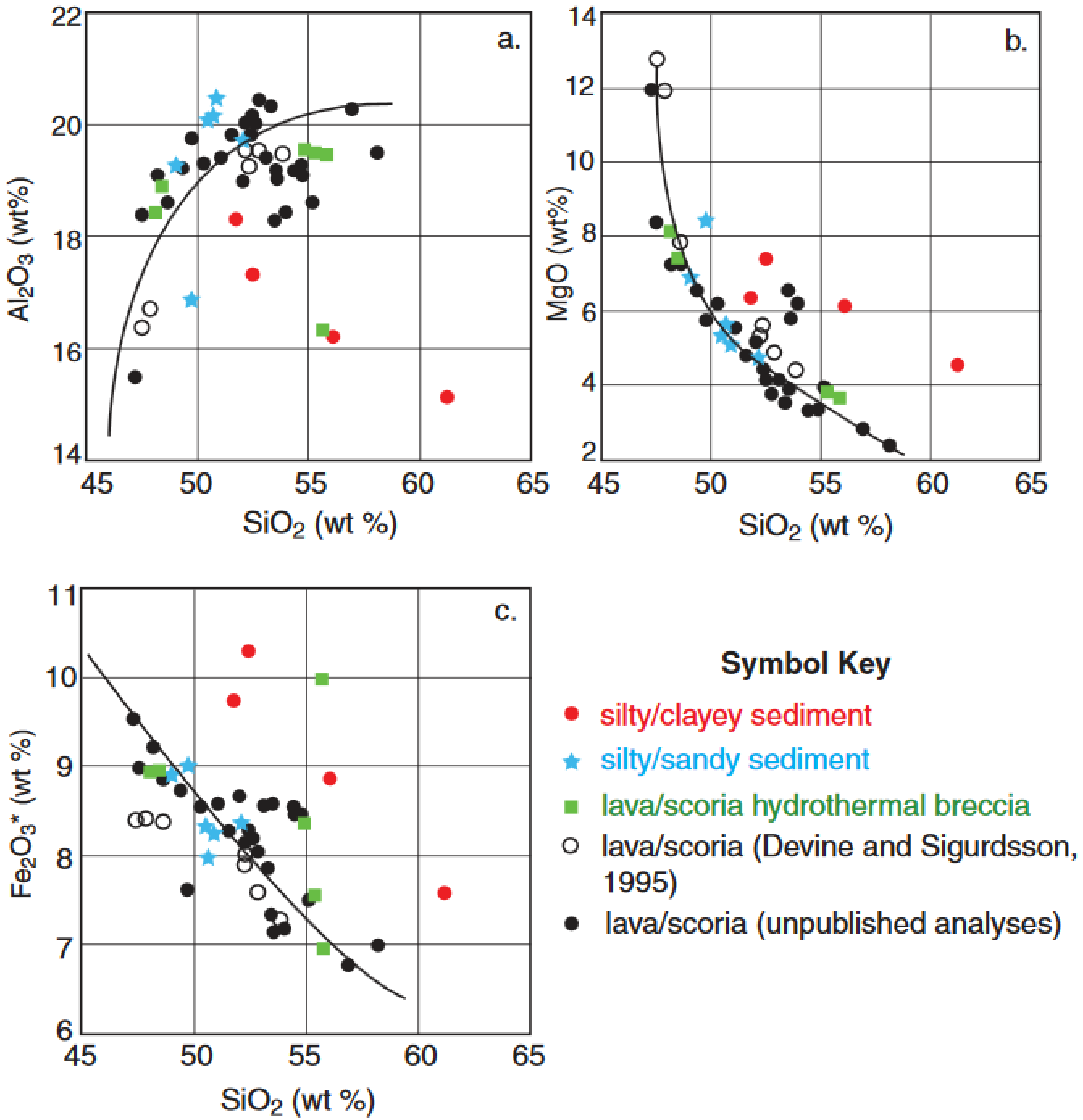
a.
b.
c.
$Al_2O_3$ (wt%)
MgO (wt%)
$Fe_2O_3$* (wt %)
$SiO_2$ (wt %)
22
20
18
16
14
12
10
8
6
4
2
11
9
7
45
50
55
60
65
Symbol Key
silty/clayey sediment
silty/sandy sediment
lava/scoria hydrothermal breccia
lava/scoria (Devine and Sigurdsson, 1995)
lava/scoria (unpublished analyses)

**Figure 11 (next page)**

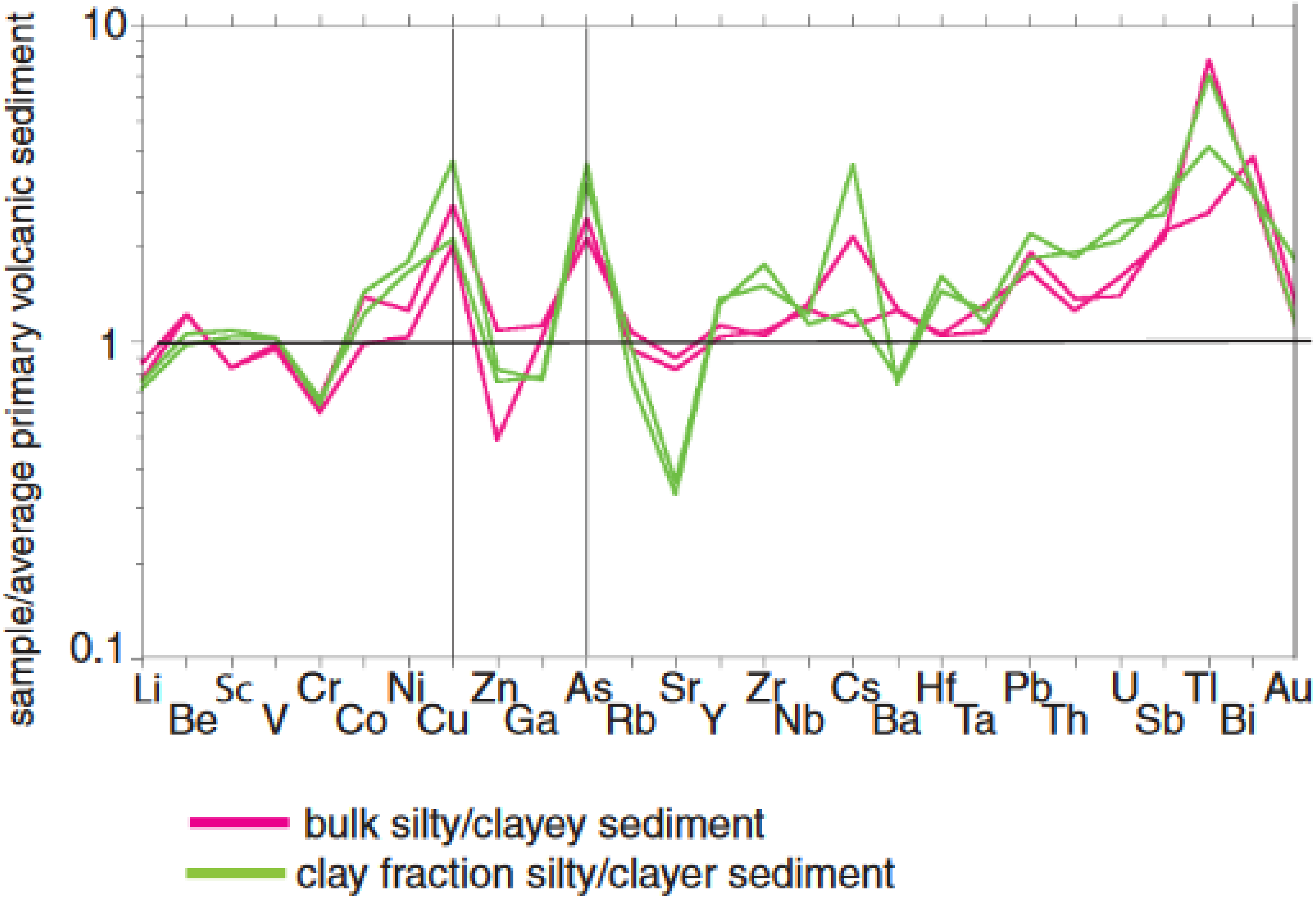

sample/average primary volcanic sediment
10
1
0.1
Li
Be
Sc
V
Cr
Co
Ni
Cu
Zn
Ga
As
Rb
Sr
Y
Zr
Nb
Cs
Ba
Hf
Ta
Pb
Th
U
Sb
Tl
Bi
Au
bulk silty/clayey sediment
clay fraction silty/clayer sediment

**Figure 12 (next page)**

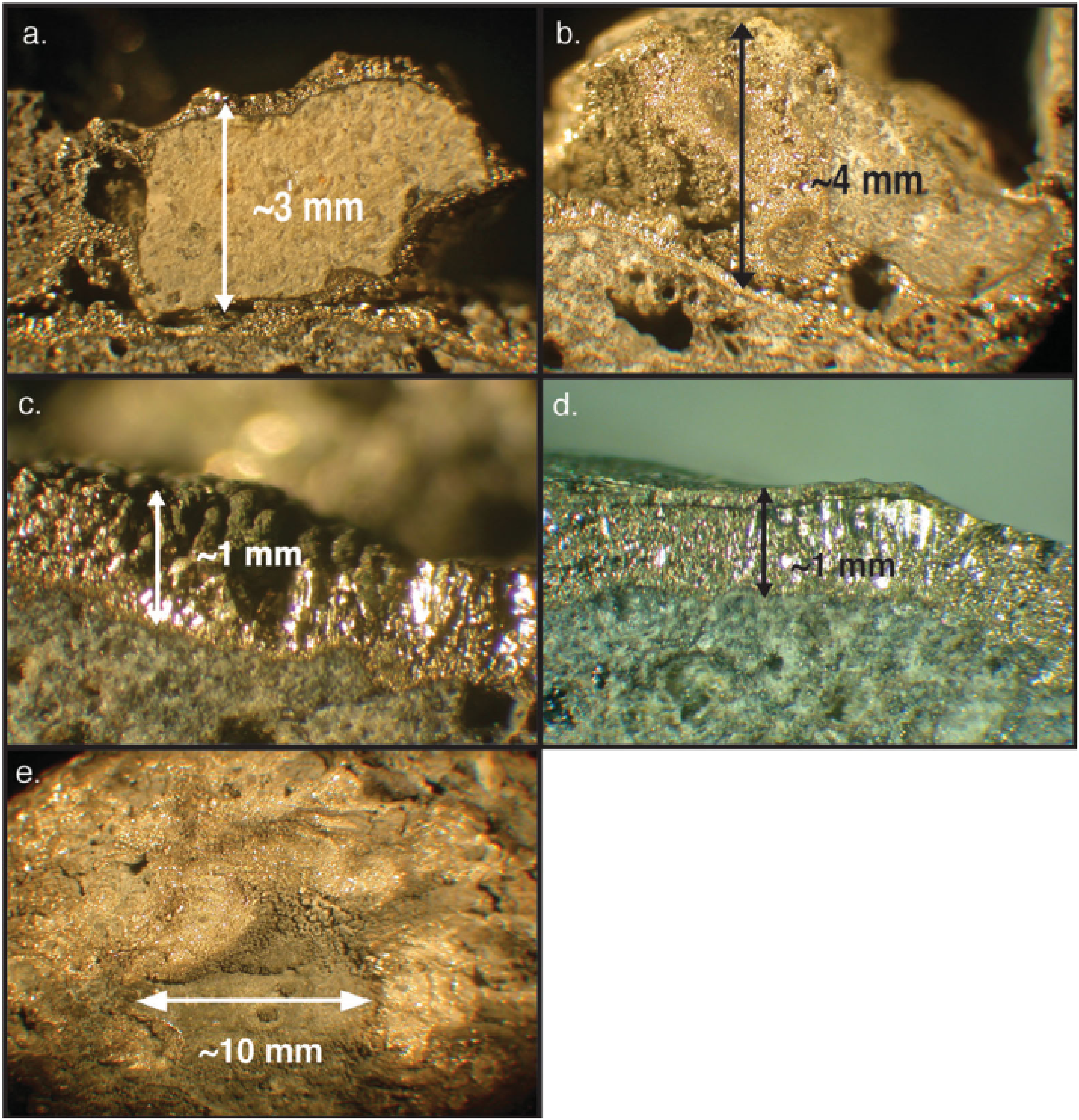
a.
~3 mm
b.
~4 mm
c.
~1 mm
d.
~1 mm
e.
~10 mm

Supporting Information for

# Hydrothermal Venting and Mineralization in the Crater of Kick'em Jenny Submarine Volcano, Grenada (Lesser Antilles)

Steven Carey, Rene Olsen, Katherine L.C. Bell, Robert Ballard, Frederic Dondin, Chris Roman, Clara Smart, Marvin Lilley, John Lupton, Brad Seibel, Winton Cornell, Craig Moyer

Graduate School of Oceanography, University of Rhode Island, Graduate School of Oceanography, University of Rhode Island, Ocean Exploration Trust, Mystic, CT, Ocean Exploration Trust, Mystic, CT, Seismic Research Centre, University of the West Indies, Graduate School of Oceanography, University of Rhode Island, Department of Ocean Engineering, University of Rhode Island, School of Oceanography, University of Washington, Pacific Marine Environmental Laboratory, NOAA, Department of Biological Sciences, University of Rhode Island, Department of Geosciences, University of Tulsa, Department of Biology, Western Washington University

## Contents of this file

Text S-1 (Details of Methods and Analytical Procedures)
Figures S-1 to S-6 (S-1 submitted separately)
Table S-1
Movies S-1 to S-6 (up loaded separately)
Captions for Figures S1 to S-6
Caption for Table S1
Captions for Movies S1 to S6

## Introduction

The supplemental data for this paper contains the following types of files: 1) text covering the details of sample collection and analytical techniques, 2) figures S1 to S7, cited within the main body of the article, 3) a table (S1) with inputs used for the geochemical modeling and the numerical results, and 4) a series of short videos (movies S1-S6) showing examples of hydrothermal venting and mineralization in the crater of Kick'em Jenny. The videos were collected using the remotely operated vehicle *Hercules* during cruise NA039 of the E/V Nautilus in October and November of 2013.

**Methods Supplemental: Details of Sample Collection and Analytical Techniques**

Gases were collected using the ROV *Hercules* and titanium gas-tight bottles outfitted with a plastic funnel that was held over the bubble streams and then triggered to collect a sample [*Edmond et al. 1992*]. Helium and neon concentrations and helium isotope ratios were determined using a special 21-cm radius mass spectrometer at the Helium Isotope Laboratory, Newport, Oregon. $CO_2$, $CH_4$, $H_2$ and other gas concentrations were determined by gas chromatography at the University of Washington. Quantitative analyses of sulfur gas species were not performed on the gas chromatograph due to analytical constraints but $H_2S$ was detected during the measurement of CH4 and the difference between the analytical total of the sample and 100% is attributed to $H_2S$ (M. Lilley personal communication). Discharge rates of gases from bubble streams on the floor of Kick'em Jenny crater were determined by holding a 2-liter plastic cylinder over narrowly focused bubbles streams with the ROV and recording the time it took to fill the cylinder. These measurements are likely to be minimum values from a particular bubble stream because cooling of the gas within the cylinder during collection resulted in some decrease in volume. We did not have the capability of measuring the temperature around the cylinder during the collection and thus are not able to quantitatively assess the extent of potential contraction. It is noted, however, that the cylinder was being held in the upward discharge of gas and hot hydrothermal fluids (max. temperature of 107° C at source) and not in direct contact with low temperature ambient seawater (~14° C). Thus cooling of the container may not have been significant during the collection time of a few minutes.

Fluids were collected in vacuum bags using a Seabird 5M pump with a PTFE head on the ROV *Hercules* and remotely triggered Niskin bottles on the side of the vehicle. Fluids were pumped through 2.5 meters of ¼" tubing. Inspection of the tubing post-collection showed that there was no precipitation with the sampling lines. Fluid densities were determined using an Anton Paar DMA 5000 M Density Meter. The instrument consists of a U-shaped borosilicate glass tube with ports for sample injection. The tube and a reference oscillator are excited to vibrate at their characteristic frequencies, where the characteristic frequency of the U-tube is a function of the density of the injected fluid. The density is then calculated internally as the quotient of the period of oscillations of the U-tube and reference oscillator.

pH measurements were carried using a Specialist Offshore Services pH probe on the *Hercules* ROV. The probe had a selectable range from 0-14 pH units and can operate up to 6000 meters waters depth. Accuracy of the measurements is 0.03 with a resolution of 0.01 pH units.

Sediment samples were characterized for both lithology and grain size. Lithology of sediment grains were determined from smear slides using a polarizing microscope and point counted on the basis of four categories: scoria (light and dark), crystals (plagioclase, amphibole, pyroxene), biogenic, and lithic. Carbonate contents were determined by coulometer. Grain size was measured using a Mastersizer2000 laser analyzer and a Hydro2000G sampler-handling unit. Sample preparation included dissolution of carbonate with 1N Acetic Acid, removal of grains >500 µm by wet sieving, and disaggregation with sodium hexametaphosphate (4g/L). Sorting and skewness parameters were evaluated using standard sedimentological calculations (Folk, 1968)

Major element compositions of samples were determined by x-ray fluorescence (XRF) using the standard BHVO-2 at the Ronald B. Gilmore X-ray Fluorescence Laboratory, University of Massachusetts. Trace element compositions were determined by Inductively Coupled Plasma Mass Spectrometer (ICP-MS) on a Thermo X-series II with collision cell technology at the Graduate School of Oceanography following the procedure in *Kelley et al.* [*2003*]. Standards used were: JB-3, BHVO-1, DNC-1, W-2, AGV-1, and EN026 10D-3. R-values of ≥0.995 were achieved for all elements reported. Arsenic measurements were collected with the collision cell on to remove Ar-Cl interference at mass 75 and enhance precision and accuracy. A standard additions test was also done for JB-3, BHVO-1, DNC-1, W-2, and EN026 10D-3 with the collision cell on get a more accurate measurement of As in those standards. Sediments were divided into a bulk fraction representative of all grain sizes and a clay fraction representative of the clay-sized fraction. Gravity separation techniques were used to separate the clay fraction from the bulk fraction. X-ray diffraction (XRD) analyses were conducted on sediment samples and hydrothermal deposits using a Rigaku XRD at the Department of Geosciences, University of Tulsa.

The morphology and major element composition of hydrothermal minerals cementing a hydrothermal breccia were determined on a Cameca SX-100 electron probe microanalyzer (EPMA) at the Department of Geosciences, Brown University from prepared thin sections. Hydrothermal minerals handpicked from sediment samples were mounted on aluminum mounts for characterization of crystal structure and texture using a JEOL (5900) scanning electron microscope (SEM) at the University of Rhode Island. The energy-dispersive spectroscopy (EDS) detector on the SEM was used for semi-quantitative determination of major elements.

To assess the nature and community structure of microbial mats at KeJ, terminal-restriction fragment length polymorphism (T-RFLP) was carried out on two samples from the inner crater. This technique gives distinct fingerprints based on restriction sites within the SSU rRNA gene. Three replicate SSU rDNA PCRs were performed as described (Davis and Moyer, 2008). These pooled amplicons were subsequently divided among eight treatments with tetrameric restriction endonucleases. All reactions were desalted using Sephadex superfine G-75 (GE Healthcare Bio-Sciences, Piscataway, NJ) and dehydrated. Reactions were separated by capillary electrophoresis using an ABI 3730 genetic analyzer with a 50-cm capillary array and POP-6 (Life Technologies, Grand Island, NY). Each reaction was separated and visualized at least twice to ensure reproducibility. Terminal-restriction fragments (T-RFs) were sized against a GeneScan 500 LIZ dye size standard (Life Technologies). Electropherograms were imported into the program BioNumerics (Applied Maths, Austin, TX). Community fingerprints were compared in BioNumerics using average Pearson product moment correlation and un-weighted pair group method with arithmetic mean (UPGMA) cluster analysis of all eight restriction digests using the relative fluorescent proportions of each electropherogram. The cophenetic correlation coefficient was calculated to assess the robustness of the cluster analysis groupings. Peak detection was limited to peaks between 50 and 500 base pairs in size and with height at least 3% of the maximum value of the fingerprint.

## Captions

**Figure S-1.** High-resolution photomosaic of the inner crater of Kick'em Jenny. Figure 1 shows the location of the surveyed area. The location of the most active gas discharging vents (Champagne and Shrimp) are marked by red stars. Note the pattern of fluid flow down the margins of the inner crater towards the relatively flat floor and the linear alignment of diffuse vent in the lower right hand side of the image.

**Figure S-2**. ROV images of a) fractured hydrothermal crusts with abundant bacterial mats on the outer crater floor and b) field of small lumpy diffuse flow vents with flocculent yellowish bacterial (red laser points are 10 cm apart).

**Figure S-3**. Composition of KeJ silty/sandy sediment (42,32,28,26,24) and silty/clayey sediment (41,40,31,18) in the grain size range 500-63 μm. Counts were normalized to the total count. a) major sediment components b) crystal components c) scoria components.

**Figure S-4**. Electron microprobe SEM photographs and analyses of pyrite overgrowths on hydrothermal breccia sample RB-03-08.

**Figure S-5.** Plot of selected trace elements and major oxides of the altered exterior of KeJ lava/scoria/breccia relative to the fresh interior.  Trace elements are in ppm.  Major oxides (Fe, S) are in wt%. RB-03-03-08 (red, solid circles), RB-03-03-17 (blue, solid squares) and RB-03-03-82 (green, diamonds).

**Figure S6.** Mass balance model for the alteration of silty/sandy sediment to silty/clayey sediment on the basis of wt% major oxides. The model composition is comprised of a portion of the silty/sandy sediment, clay minerals, and 1 wt% pyrite. Values for major oxide composition of the clay minerals are from the literature (see text). RB-03-03-28 is the starting silty/sandy volcanic sediment and RB-03-03-18 is the alteration product used in the calculation for comparison with the model.

**Table S1.** Mixing model to assess hydrothermal alteration of silty/sandy volcanic sediment at Kick'em Jenny.

**Movie S1.** ROV video of fragile Fe-oxyhydroxide hydrothermal vents on the southeast wall of the inner crater of Kick'em Jenny volcano. Water depth 252 meters. Collected on 11/01/2013.

**Movie S2.** ROV video of white hydrothermal streams on the eastern wall of the inner crater of Kick'em Jenny volcano. Water depth ~260 meters. Collected on 11/01/2013.

**Movie S3.** ROV video of friable hydrothermal tubular mounds near the rim of the inner crater of Kick'em Jenny volcano. Water depth ~235 meters. Collected on 11/01/2013.

**Movie S4.** ROV video of gas collection at Champagne hydrothermal vent in the inner crater of Kick'em Jenny volcano. Water depth ~265 meters. Collected on 11/02/2013**.**

**Movie S5.** ROV video of gas flux measurement using an inverted plexiglass container at the Champagne hydrothermal vent in the inner crater of Kick'em Jenny volcano. Water depth ~265 meters. Collected on 11/13/2013.

**Movie S6.** ROV video of yellowish bacterial mat at the summit of Kick'em Jenny volcano. Water depth ~200 meters. Collected on 11/13/2013.

**References**

Davis, R. and C. Moyer (2008), Extreme spatial and temporal variability of hydrothermal microbial mat communities along the Mariana Island Arc and southern Mariana back-arc system, Jour. Geophys. Res., 113, B08S15, doi:10.1029/2007JB005413.

Edmond, J., G. Massoth, and M. Lilley (1992), Submersible-deployed samplers for axial vent waters. *Ridge Events 3 (1)* 23-24.

Folk, R.L. (1968), Petrology of Sedimentary Rocks. Hemphill's, Austin, Texas, 170 pp.

Kelley, K. A., T. Plank, J. Ludden and H. Staudigel (2003), Composition of altered oceanic crust at ODP Sites 801 and 1149, *Geochem. Geophys. Geosys. G3, 4(6),* 1-21.

Additional supporting materials available at
http://onlinelibrary.wiley.com/doi/10.1002/2015GC006060/abstract